Distribution and Mobility of Platinum-Group Elements in the Late Cretaceous Ni-laterite Soil in the Northern Oman Mountains

Salah A. Al-Khirbash[a+] and Ahmed H. Ahmed[b,c]

[a] Department of Earth Sciences, Sultan Qaboos University, Muscat, Oman

[b] Faculty of Earth Science, King Abdulaziz University, Jeddah 21589, Saudi Arabia

[c] Department of Geology, Faculty of Science, Helwan University, Cairo, Egypt

[+]corresponding author: S. Al-Khirbash (khirbash@squ.edu.om)

Abstract

Low-grade Ni-laterite deposits are well-developed over the mafic/ultramafic protoliths in the northern Oman Mountains. Concentrations, distribution patterns and mobility of platinum-group element (PGE) are investigated in some Ni-laterite profiles of the Oman ophiolite as a possible unconventional PGE resource. The highest PGE contents (up to 253 ppb) in the Oman Ni-laterites are mainly concentrated in the oxide/clay-rich zone of the laterite profiles. The PGE contents are substantially decreased toward the saprolite and underlying protoliths (average total PGE = 35 ppb). The highest PGE content in the oxide zone is mostly corresponding to Pt > Ru > Pd, while the lowest PGE content is mostly corresponding to Os < Rh < Ir, which shows a general positive trend of PGE distribution patterns. There is a general positive correlation between PGE contents and both Cr_2O_3 and Fe_2O_3 contents in the Ni-laterite profiles. This may reflect the formation of PGE-Fe nanoparticle alloys that are hosted by Fe-rich oxyhydroxides or due to the residual accumulation of chromite in the oxide/clay-rich zone during the lateritization process. The PGE distribution patterns and positive correlation with the ultramafic index of alteration (UMIA) indicate that PGE can be mobilized in different proportions in the surficial environment upon progressive lateritization processes. The high concentration of total PGE in the Oman Ni-laterite is in good agreement with the PGE-rich laterite deposits worldwide, which can be considered as an unconventional PGE resource if adequate extraction and refining processes can be applied for their recovery from the possible upcoming Ni production.

Keywords: Ni-laterite, platinum-group elements (PGE), ultramafic index of alteration (UMIA), Oman ophiolite

1. Introduction

Platinum-group elements (PGE) are considered among the so-called critical metals which are essential for the high technological industry. However, the conventional PGE deposits (e.g., stratiform chromitite and magmatic sulfide deposits) from which these metals can be extracted are very limited in the world. The oxidation and supergene enrichment process, also known as the lateritization process, is a chemical weathering resulting in the dissolution, transportation, and redistribution of valuable metallic elements at or near the Earth's surface. Laterite profiles produced by pervasive chemical weathering of mafic/ultramafic rocks were known to be an important source of metallic deposits such as nickel (Ni), cobalt (Co), and iron (Fe), which are known in literature as Ni-laterites (Evans, 1993; Freyssinet et al., 2005; Golightly, 2010; Thorne et al., 2012a, 2012b; Butt & Cluzel, 2013; Reich & Vasconcelos, 2015). This supergene enrichment process is also one of the important processes for residual and secondary enrichment of PGE and gold in these mineral deposits (Bowles et al., 1994; Gray et al., 1996; Varajão et al., 2000; Traoré et al., 2008; Aiglsperger et al., 2015, 2016, 2017; Rivera et al., 2018; Tobón et al., 2020). There is a consensus that three main processes are possibly controlling the PGE concentration and distribution in terrestrial rocks. They are partial melting, crystal fractionation, and post-magmatic alteration (Barnes et al., 1985). Platinum (Pt) and gold (Au) are more mobile than the other PGE during the alteration processes, while palladium (Pd) might be mobilized by hydrothermal fluids (e.g., Keays et al., 1981, 1982; Barnes et al., 1985; Stumpfl, 1986). High concentrations (~ 4 ppm) of PGE and Au are reported from some Ni-laterite deposits such as those in Acoje (Philippines) and Musongati and Kapalagulu (Burundi) laterites (Bandyayera, 1997). These may add values to the lateritization processes as a potential agent for PGE accumulation via chemical weathering of mafic/ultramafic rocks. Despite that, the effect of lateritization on PGE enrichment and platinum-group minerals (PGM) accumulation is still a matter of debate. In some places, PGE-rich (about 3 ppm) with accumulation of various types of PGM have been previously reported from Ni-laterites in the Falcondo laterite deposit of the Dominican Republic, which might be attributed to the presence of small chromitite pods associated with serpentinized dunite (Proenza et al., 2007; Zaccarini et al., 2009; Proenza et al.,

2010; Aiglsperger et al., 2015). Although the Ir-subgroup (IPGE = Os, Ir, and Ru) is considered to be highly resistant than the Pd-subgroup (PPGE = Rh, Pt, and Pd) under the surficial conditions, several authors recognized that IPGE can also be mobilized under hydrothermal and/or lateritic weathering conditions (Stockman & Hlava, 1984; Garuti & Zaccarini, 1999; Zaccarini et al., 2005; Garuti et al., 2007, 2012). The lateritization process is occasionally producing secondary PGE alloys, sulfides, sulfarsenides, and/or oxides/hydroxides by alteration of primary magmatic PGM precursors (Cornelius et al., 2008; Ndjigui & Bilong, 2010). However, supergene formation of PGM without the presence of magmatic PGM precursors has previously been reported from the platiniferous Au-Pd belt of Minas Gerais of Brazil (e.g., Cabral et al., 2009, 2011).

The Oman ophiolite represents one of the best-preserved oceanic lithospheres in the world, where a complete sequence of ophiolite stratigraphy is well-preserved and exposed from the upper mantle to the upper crust. The mantle sequence of the Oman ophiolite is essentially composed of tectonized harzburgite with minor dunites, lherzolites, and chromitites (Roberts, 1986). The mineralogical classification and general chemical characteristics of some Ni-laterite profiles from the northern mountains of the Oman ophiolite were previously studied to characterize the mineralization zones and their economic importance (Al-Khirbash, 2015, 2016, 2020; Al-Khirbash et al., 2014). The chromitite deposits of the Oman ophiolite were found to contain high concentration of PGE (Ahmed & Arai, 2002) and various types of PGM, which mainly comprised IPGE sulfides and, to a lesser extent, sulfarsenides (Ahmed & Arai, 2003). Oxidation of primary PGM sulfides into oxides is also described at low temperature conditions in the Oman ophiolitic chromitites (Ahmed et al., 2002). Desulfurization/oxidation is the main process in the surface environments that is responsible for the transformation of primary PGE sulfides into oxides and PGE-Fe alloys. To constrain the PGE distribution patterns, mobility, and concentration in supergene surficial environments, their distribution in the Ni-laterite of the Oman ophiolite is thoroughly studied in the present research. In this contribution, a detailed bulk-rock analysis and PGE geochemistry from six different Ni-laterite profiles of the Northern Oman Mountains is thoroughly studied with the aim to understand the behavior, distribution, and mobility of PGE in the oxidation and supergene environments. A comparison with world-class

laterite deposits is also done to assess the economic potentiality of the PGE in the Oman Ni-laterites.

2. Geologic settings

The present study is located at about 180 km SW of Muscat and lies around Saqah town between N 22^{o} 45` and $22^{o}$ 50` and 58^{o} 40` $58^{o}$ 50` (Figure 1a). The area is covered by the Late Cretaceous allochthonous ultramafic/mafic rocks of the Semail ophiolite nappe that was emplaced as a result of the obduction of the Tethyan rocks onto Middle Permian to Middle Cretaceous shelf carbonate sequences of the Arabian passive continental margin (Glennie et al., 1974; Coleman, 1981; Boudier et al., 1985; Dercourt et al., 1986; Lippard et al., 1986; Skelton et al., 1990; Searle & Cox, 2002; Peters et al., 2005; Searle, 2019). Small outcrops exposed on the eastern part of the study area consist of the deep marine limestone, adiolarian chert, and pelagic sediments (Hawasina window) and low-grade epidote greenschist facies metasedimentary rocks, cherts, marbles, and quartzites (metamorphic sole) (Cowan et al., 2014) (Figure 1b).

The Ni-laterites from the Northern Oman Mountains are part of the Maastrichtian neo-autochthonous post-obduction terrigenous clastic facies (Qahlah Formation) and lie unconformably on the obducted Semail ophiolite while they are capped by post-obduction Late Campanian/Maastrichian–Tertiary sedimentary rocks of the Simsima formation (Abbasi et al., 2014). The presence or absence of the laterite soil in the Northern Oman Mountains might reflect the original irregular paleotopography, the existence of basins associated with syn-sedimentary structures, and the prevailing climatic conditions at the end of the Cretaceous Period that all initiated an intense and prolonged weathering process of the ophiolite (Nahon et al., 1982; Nolan et al., 1990; Al-Khirbash et al., 2010).

Six laterite localities (1 to 6) have been investigated (Figure. 1b). Based on field work and mineralogical and physical characteristics, the studied laterite soil in the Northern Oman Mountains can be grouped into two main zones: the protolith zone and the laterite zone (Figure 2). The protolith consists of either layered gabbro or serpentinized peridotite in the most localities (Figures 2, 3a, 3b). The laterite zone comprises the green to grayish saprolite horizon, the reddish to brown massive to pisolitic oxide horizon, the upper ferricrite/ironstone horizon,

and in some localities the compact clay horizon (Figures 2, 3c, d, e). A detailed field and mineralogical description of these zones was given by Al-Khirbash (2015, 2016).

3. Sampling and analytical techniques

Twenty-five samples were collected from six lateritic profiles in the Oman Mountains, (Figure 2). Samples were selected based on the mineralogical and geochemical characteristics of previous studies (Al-Khirbash, 2015, 2016), particularly those which showed high concentration of Cr-Ni-Co elements. The rock samples were broken into small chips using a hydraulic rock splitter and then pulverized using a Fritsch Pulverisette 5 planetary mill for 30 to 45 minutes. Samples up to 60 g in size are fire assayed using a nickel sulfide (NiS) fire assay Neutron Activation Analysis (INAA) procedure. The nickel sulfide button is dissolved in concentrated HCl, and the resulting residue which contains all the PGE and Au are collected on a filter paper. This residue undergoes two irradiations and three separate counts to measure all the PGE and Au. One batch of 34 samples includes two blanks, three certified standards, and three duplicates. Detection limits are as follows: Os (2 ppb), Ir (0.1 ppb), Ru (5 ppb), Rh (0.2 ppb), Pt (0.5 ppb), Pd (2 ppb), and Au (0.5 ppb). All analyses were carried out at Activation Laboratories Ltd. (Ancaster, Ontario, Canada). Bulk major oxide geochemistry of the studied samples was taken partly from a previous study by Al-Khirbash (2016).

4. Petrography

Microscopic studies of the protoliths showed that the layered gabbro consists of fresh to altered plagioclase crystals with some altered pyroxenes (Figure 4a), and the serpentinized peridotites consist of pyroxene crystals that are altered to lizardite and chrysotile (Figure 4b). The above saprolite horizon comprises compact gray-greenish color rocks with abundant light-green lizardite and chrysotile minerals and commonly contain carbonate-filled fractures (Figure 4c). The oxide horizon is predominantly composed of hematite and goethite with rounded and ellipsoidal pisolite appearance (Figure 4d). The upper ferricrite/ironstone horizon consists mainly of massive hematite, goethite with magnetite, and inherited chromite grains that are replaced by hematite and authigenic chlorite (Figures 4d, e). XRD data confirmed the presence of these minerals (Figure 5).

5. Geochemistry

5.1 Major and compatible trace element geochemistry

Based on mineralogical characteristics as well as variations in physical properties such as texture, structure, and color, the laterite profiles of the Oman ophiolite can be classified into three categories: (1) protolith, which is represented by layered gabbro or serpentinized peridotites; (2) saprolite, which is the partly weathered zone overlying the protolith; and (3) oxide/clay-rich zone, which represents the uppermost part of the laterite profiles. Geochemically, there are slight differences in major and compatible trace elements contents between the protolith and saprolite zones. Thus, they will deal together in the following descriptions. On the other hand, the oxide/clay-rich zone shows significant geochemical differences compared with the protolith and saprolite zones. The major and selected compatible trace elements composition of the protolith, saprolite, and oxide/clay-rich zones of the studied laterite profiles is shown in Tables 1 and 2.

5.1.1 Protolith and saprolite zones

The Ni-laterite profiles of the Oman Mountains are essentially well-developed over serpentinized peridotites and/or over layered gabbros (Figure 2). The major outcome of the serpentinization process of ultramafic rocks is the addition of water into the system, where serpentinized peridotites can contain more than 13 wt.% of water in the produced hydrous mineral crystal structure (e.g., Deschamps et al., 2013). However, a careful description of the samples should be done because the loss on ignition (LOI) is not always correlated with the degree of serpentinization since the presence of other hydrous phases such as talc, brucite, chlorite, and clay minerals can influence this budget. Careful petrographic investigation and X-ray diffraction (XRD) analysis of the studied serpentinized peridotite protolith of the Oman laterite profiles confirm the absence of such hydrous minerals, except the lizardite, antigorite, and clinochrysotile that represent the major mineral phases in the studied serpentinized peridotite protolith (Al-Khirbash, 2016). The peridotite protolith of all laterite profiles shows the same compositional ranges in terms of their LOI and major and compatible trace elements constituents. The LOI of the peridotite protolith varies from 14.60 wt.% to 16.18 wt.%, with an average of 15.52 wt.% (Table 1). The low CaO content (0.05–3.22 wt.%, with an average 1.30 wt.%) in the serpentinized peridotites revealed that serpentinization is the only process affecting the peridotite

protolith. The LOI in the saprolite zone shows comparable values to the underlying serpentinized peridotites, varying from 14.59 wt.% to 15.88 wt.%, with an average of 15.27 wt.%, and a similar range of CaO content (Table 1). The common major oxides (SiO_2, MgO, Fe_2O_3, and Al_2O_3) do not show significant differences between the peridotite protolith and the overlying sparolite zone, where the average contents of these components are 37.22 wt.%, 35.85 wt.%, 7.85 wt.%, and 1.04 wt.%, respectively, in the former and 38.69 wt.%, 35.96 wt.%, 7.77 wt.%, and 0.75 wt.%, respectively, in the latter (Table 1). The most compatible trace elements (e.g., Cr_2O_3, NiO, Co_3O_4, and MnO) show comparable values in both the saprolite zone and the underlying peridotite protolith. The average NiO and Co_3O_4 contents in the saprolite zone (0.28 wt.% and 0.01 wt.%, respectively) are relatively higher than those in the underlying peridotite protolith (0.18 wt.% and 0.01 wt.%, respectively) (Table 1). The Cr_2O_3 and MnO contents are almost similar in the peridotite protolith and in the saprolite zone. They are averaging 0.34 wt.%, 0.30 wt.%, and 0.35 wt.%, respectively (Table 1).

5.1.2 Oxide/clay-rich zone

The upper oxide and clay-rich zones of the laterite profiles show significant differences in terms of the LOI, major constituents, and compatible trace elements compared with their protolith and saprolite zones. In terms of the major constituents, the distinguishing feature of these uppermost parts of the laterite profiles is the substantial increase in Fe_2O_3 and Al_2O_3 contents and the extremely leaching of SiO_2 and MgO contents compared with the underlying protolith and saprolite zones. The laterite profile at locality #1 seems to be the most highly weathered profile. It is highly carbonated where the CaO and LOI contents reached up to 30.31wt.% and 25.62 wt.%, respectively (Table 2). Except for the profile at locality #1, the oxide and clay-rich zones of the other laterite profiles show comparable data of wide compositional ranges in terms of their major and compatible trace element constituents. SiO_2 is the most prominent component that is progressively decreased from the protolith to the uppermost oxide/clay-rich zones. It displays reverse correlation with both total iron, as Fe_2O_3, and Al_2O_3 contents (Figures 6a, b). The SiO_2 content varies from 27.06 wt.% in the less lateritized samples down to 2.23 wt.% in the strongly lateritized ones (Table 2). The total iron, as Fe_2O_3, is highly increased with the increasing degree of lateritization. It varies from 16.82 wt.% in the less weathered samples up to 85.5 wt.% in the highly weathered ones (Figure 6a). The Al_2O_3 content shows the highest value in the clay-rich

zone, where it reaches up to 24.49 wt.%, and the lowest Al_2O_3 value (1.70 wt.%) is in the oxide-rich zone (Figure 6b). The MgO content, on the other hand, is the most leachable component in the oxide/clay-rich zone of the laterite profiles. It is reduced to 0.37 wt.% in the highly lateritized samples and to 6.18 wt.% in the least lateritized ones (Figures 6c, d). The MgO content shows strong positive and negative correlations, respectively, with SiO_2 (Figure 6c) and Fe_2O_3 (Figure 6d). In terms of the compatible trace elements (Cr, Ni, Co, and Mn), they are highly (Cr and Ni) to slightly (Co and Mn) enriched in the oxide/clay-rich zones of the laterite profiles compared with the protolith and saprolite zones (Table 2). The Cr_2O_3 content is the most enriched compatible component in the uppermost oxide/clay-rich zone, where it reaches up to 11.44 wt.% (3.79 wt.% on average). Similarly, the NiO content in the oxide/clay-rich zone of the laterite profiles reaches up to 2.85 wt.% (1.07 wt.% on average). It is more or less positively correlated with Fe_2O_3 and Al_2O_3 contents (Table 2 and Figure 7a). The Co_3O_4 and MnO contents also relatively increase in the oxide/clay-rich zone, which reach up to 0.50 wt.% and 2.52 wt.%, respectively (0.11 wt.% and 0.36 wt.% on average), showing a good positive correlation with NiO and Fe_2O_3 contents (Table 2).

5.2 Platinum-group elements (PGE) geochemistry

5.2.1 Protolith and saprolite zones

The PGE contents in the serpentinized peridotite and the saprolite zone are almost similar, with very limited variations (Table 1). The total PGE content of the serpentinized peridotite protolith ranges between 31 and 41 ppb (35 ppb on average), which shows approximately flat chondrite-normalized PGE distribution patterns (Figure 8a) with slight positive fractionation ratios (average Pd/Ir_N and Ru/Pt_N = 1.76 and 0.95, respectively). It is noteworthy that the total IPGE (= Os, Ir, and Ru) is progressively increased along with the increase of PPGE (= Rh, Pt, and Pd) from the protolith to the saprolite and then to the oxide/clay-rich zones of the laterite profiles (Figure 8b). The saprolite samples of laterite profiles show relative enrichment in total PGE compared with the serpentinized peridotites, varying from 30 to 91 ppb (55 ppb on average), but with pronounced positive trend from Os to Ru and then depletion in Rh and positive again from Pt to Pd of the PGE distribution patterns (Table 1 and Figure 9b). The Pd/Ir_N and Ru/Pt_N fractionation ratios reflect the relative enrichment in the IPGE compared with the PPGE. The average ratios in the saprolite samples are 1.94 and 1.53, respectively. The Au content in the

peridotite protolith and saprolite zones is approximately similar, which varies from 1 up to 5 ppb (Table 1).

5.2.2 Oxide/clay-rich zone

The total PGE content in the oxide/clay-rich zone of the laterite profiles is comparatively very high with those in the protolith and saprolite zones. The enrichment factor reaches up to six times in the oxide/clay-rich zone. Total PGE content varies from 57 up to 253 ppb, with an average of 136 ppb (Table 2). Both IPGE and PPGE sub-groups are substantially increased in the oxide/clay-rich zone of the laterite profiles, showing a general positive trend from Os to Pd in the chondrite-normalized PGE distribution patterns (Figures 9b–d), except for the profile at locality #1, which shows erratic PGE distribution patterns (Figure 9a). There is an obvious enrichment in the total PGE contents, with promotion of the lateritization process from the protolith upward to the uppermost oxide and clay-rich zones, which is reflected by the substantial increase in Fe_2O_3, Cr_2O_3, and NiO contents (Figures 7b–d). The Pd/Ir_N and Ru/Pt_N ratios also reflect the general increase in both IPGE and PPGE in the PGE distribution patterns, which vary respectively from 0.45 to 3.81 (1.43 on average) and from 0.51 to 7.75 (2.78 on average). The ∑IPGE/∑PPGE ratio varies from 0.3 to 0.86 (0.61 on average) in the peridotite protolith, from 0.52 to 2.11 (1.12 on average) in the saprolite, and from 0.31 to 2.18 (1.16 on average) in the oxide/clay-rich zone, which reflects a progressive increase of both IPGE and PPGE upward from the protolith to the oxidized zone of the laterite profiles (Figure 8b). Osmium (Os) has the lowest values in all laterite profiles (Figures 9a–d). It is almost around the detection limit of the analysis, which is most probably due its volatile nature in the surficial environment. On the other hand, Ru shows the highest values among the IPGE metals in all laterite profiles, showing pronounced positive anomalies, which is most probably due to its presence as laurite, or as a Ru-Ir-Fe alloy, in the accumulated chromian spinel in the saprolite and oxide/clay-rich zones (Figures 9a–d). In the PPGE subgroup, Pd has the highest values in all laterite profiles (Figures 9a–d), except in a few samples in localities #1 and # 6, where Pt has the highest metal content among the PPGE (Figures 9a, d). The Au content in the oxide and clay-rich zones is relatively higher than those in the protolith and saprolite zones. It reaches up to 15 ppb in the clay-rich zone (Table 2).

6. Discussion

6.1 Degree of lateritization

When the mafic/ultramafic rocks are exposed to the surface, they undergo intense chemical and mechanical weathering processes, which are mainly controlled by climatic and topographic conditions (Golightly, 1981, 2010; Freyssinet et al., 2005). These oxidation and supergene processes lead to the leaching of major elements (i.e., MgO and SiO_2) from the ferromagnesian minerals (olivine and pyroxenes) in parent rocks, whereas other elements (e.g., Ni, Mn, and Co) can be enriched up to the economic values (Aiglsperger et al., 2016). Water-insoluble metals such as Fe_2O_3, Al_2O_3, and Cr_2O_3 are also residually accumulated in situ as oxides and oxyhydroxides, which play an important role as metals-retention phases in the uppermost part of the laterite profiles (Butt & Cluzel, 2013; Bowles et al., 2017). To evaluate the degree of lateritization and chemical changes in ultramafic rocks during the formation of Ni-laterite, Aiglsperger et al. (2016) defined a factor called ultramafic index of alteration (UMIA), which is mainly based on the index of lateritization (IOL) proposed by Babechuk et al. (2014). The UMIA is calculated using the molar ratios of the major element oxides from the wt.% contents of the whole rock analysis (Duzgoren-Aydin et al., 2002), and the IOL is calculated as the wt.% of the major oxides (Babechuk et al., 2014; Aiglsperger et al., 2016; Tupaz et al., 2020). The following equations are used to calculate the UMIA and IOL:

$$UMIA = 100 \times [(Al_2O_3 + Fe_2O_{3(T)})/(SiO_2 + MgO + Al_2O_3 + Fe_2O_{3(T)})]$$

$$IOL = 100 \times [(Al_2O_3 + Fe_2O_{3(T)})/(SiO_2 + MgO + Fe_2O_{3(T)})]$$

These weathering indexes depend on the composition of ultramafic rocks (i.e., peridotites) that are essentially dominated by MgO and SiO_2, with negligible amounts of CaO, Na_2O, and K_2O (Babechuk et al., 2014). The breakdown of primary minerals is occasionally followed by the development of secondary minerals such as serpentine, chlorite, clay minerals, and oxyhydroxide phases (e.g., Fe-Mn oxides and hydroxides) (Rivera et al., 2018). Thus, the values of UMIA and IOL indexes give important information about the weathering trend of ultramafic rocks, which can also be shown as ternary diagrams of A-SM-F [$(Al_2O_3$-$(SiO_2$+MgO)-Fe_2O_3] and AF-S-M [$(Al_2O_3$+$Fe_2O_3)$-SiO_2-MgO] (Figures 10a, b), and the IOL is shown as ternary S-A-F (SiO_2-Al_2O_3-Fe_2O_3) ternary diagram (Figure 10c). The UMIA of the ultramafic protolith of the Oman Ni-laterite ranges from 3% to 5%, with an average of 4%, and the less weathered saprolite samples are more or less similar to the underlying protolith where the values of UMIA vary from

3% to 4% (Figure 10a). The oxide/clay-rich zone of the laterite profiles has UMIA values between 38% and 89%, with an average of 70% (Figures 10a, b). The IOL, on the other hand, is comparable with the UMIA values, where the average values in the protolith, saprolite, and oxide/clay-rich zones are 4%, 4%, and 79%, respectively (Figures 7a–c). Except one sample from locality #1 where the Al_2O_3 content is exceptionally high, the Ni-laterite profiles of the Oman ophiolite are characterized by constantly high Fe/Al ratios (Figures 10a–c and Table 2).

It is obvious that both Al_2O_3 and Fe_2O_3 contents are progressively increased with the increasing degree of lateritization (i.e., UMIA) toward the surface of the laterite profiles. There is a good direct relationship between the two components, from the ultramafic protolith to the oxide/clay-rich zones (Figure 11a). The Ni and Co, which are mainly hosted by ferromagnesian minerals (e.g., olivine and pyroxenes) in the parent rocks, are also progressively increased with the increasing degree of lateritization (Figure 11b), as concluded by Al-Khirbash (2016), and are hosted by goethite, chlorite, kaolinite, and other Ni-bearing serpentine and talc (Al-Khirbash 2015). The residual accumulation of chromite in the uppermost part of laterite profiles is also obvious, which clearly increases with the increasing process of lateritization (Figure 11c). This is also clearly shown by the increase of total PGE with the increase in Cr_2O_3 contents in the laterite profiles. This is because chromite is considered as one of the main hosts of PGE in general and IPGE in particular (Figures 8a–8d). Based on the calculated UMIA and IOL values, the Oman Ni-laterite are in a good agreement with the moderately lateritized profiles worldwide (Babechuk et al., 2014; Rivera et al., 2018).

6.2 PGE enrichment in Ni-laterite

In general, the total PGE contents in Ni-laterites around the world are ranging between ≤ 100 ppb and up to few hundreds ppb in concentration (Augé & Legendre, 1994; Eliopoulos & Economou-Eliopoulos, 2000; Ndjigui & Bilong, 2010; Aiglsperger et al., 2015, 2016; Rivera et al., 2018). However, in some places, exceptionally enriched lateritic crusts with 2 ppm, as well as more than 4 ppm total PGE, were reported in the Ora Banda Sill in Western Australia (Gray et al., 1996) and in Burundi (Maier et al., 2008). In all of the studied Ni-laterite profiles from the Northern Oman Mountains, the uppermost oxide/clay-rich zone shows the highest PGE contents compared with the saprolitic zone and the underlying serpentinized peridotite/layered gabbro protolith. The selective concentration of PGE contents in the upper levels of the weathering

profile, compared with their initial low concentrations in the underlying bedrocks, as well as the positive correlation between the UMIA and total PGE contents (Figure 11d), indicate that PGE can be mobilized in different proportions throughout the weathering profile (e.g., Aiglsperger et al., 2016; Rivera et al., 2018; Tobón et al., 2020). From the PGE distribution patterns (Figures 9a–d), it is clearly shown that Ru, Pt, and Pd are more mobile than Ir and Rh, while Os shows the lowest resistant metal in the supergene surficial environment where it is mostly leached out from the weathered profiles. The pronounced Ru positive anomalies from all of the studied laterite profiles are mostly attributed to its presence as laurite (RuS_2) crystals, or as Ru-Fe alloys, within the residually accumulated chromite grains in the weathered laterite profiles. Although PGM grains were not reported from the studied Ni-laterite profiles (it needs more careful observations under high magnifications), it is confirmed from previous studies on the Oman ophiolite where the main PGE mineralogy are laurite in the primary chromite (Ahmed & Arai, 2003) and PGE oxides in weathered lithologies (Ahmed et al., 2002). The PGE mobility in surficial environments can be attributed to the lateritization processes that resulted in the migration of these metals toward the oxide and oxyhydroxide zones (Eliopoulos & Economou-Eliopoulos, 2000; Talovina & Lazarenkov, 2001; Ndjigui & Bilong, 2010; Aiglsperger et al., 2015). The possible controlling factors of PGE mobility and redistribution within the laterite profile are (1) the Eh–pH ratio of the weathering solutions, (2) the Cl concentration in the laterite profile, and (3) the mode of occurrence of PGM in the parent rocks before weathering (Bowles et al., 1994a, 1994b; Salpéteur et al., 1995; Ahmed & Arai, 2002, 2003; Ahmed et al., 2002). In addition to the Pt-Pd-Cl complexes, the Pt and Pd as redox metals can also be mobilized as inorganic complexes in low temperature conditions (Colombo et al., 2008). The highly accumulated chromite grains in the uppermost part of the weathered profiles of the Oman ophiolite (Figure 11c) could be accompanied by the enrichment of total PGE, in general, and IPGE, in particular. The IPGE, which have higher melting points than the PPGE, tend to be concentrated in refractory phases (i.e., chromite) and in early cumulates relative to PPGE, which are more incompatible and tend to be retained in the residual melt and crystallized with the interstitial sulfide phase (Barnes et al., 1988; Edwards, 1990; Prichard et al., 1996a, 1996b). Thus, PPGE could be easily mobilized and redistributed during the chemical weathering of parent rocks than the IPGE, which are mainly related to the chromite accumulation. Both mechanisms, the leaching of PPGE from the

interstitial sulfide phase and the accumulation of IPGE with chromite, will lead to the increase in both of them in the oxide zone of the laterite profiles (Figure 8b).

Previous studies on the mobility of PGE during lateritization processes revealed that acidic conditions (pH < 6 and Eh > 0.4) could lead to the dissolution of PGE-bearing minerals, especially PPGE phases, and then they would undergo subsequent transportation in solution and accumulation in the oxidized Fe-rich laterite profiles (Plimer & Williams, 1988; Bowles et al., 1994a, 1994b; Talovina & Lazarenkov, 2001). The PGE are accumulated as PGE-rich alloys, which coprecipitate with Fe and Mn oxides under such acidic conditions (Bowles et al., 1994a, 1994b; Salpéteur et al., 1995; Ndjigui & Bilong, 2010; Tobón et al., 2020). Complex Pt-Ir-Fe-Ni alloys were recently found as inclusions and packed nanoparticles within pore spaces of Fe oxides and oxyhydroxides of the Loma Peguera Ni-laterite deposit in the Dominican Republic (Aiglsperger et al., 2015, 2016) and in the Planeta Rica Ni-laterite profiles of Northern Colombia (Tobón et al., 2020). These observations are in good agreement with the previous studies, which indicated that the high concentrations of Pt, Pd, and Ru, as well as the transition metals such as Ni, Co, Cu, and Zn, in laterite profiles, are essentially hosted by secondary minerals like Fe-oxy-hydroxides or smectite clay minerals (Oberthür & Melcher, 2005; Ndjigui & Bilong, 2010). The high total PGE contents in the oxide/clay-rich zone of the Oman Ni-laterite profiles are in accordance with this idea and could be accumulated as PGE-Fe alloys that co-precipitated with oxides and oxyhydroxides. The newly formed supergene PGE alloys could be formed in situ during serpentinization and/or lateritization processes by dissolving the primary magmatic PGM precursor (Aiglsperger et al., 2016).

6.3 Possible economic potentiality

Although the total PGE contents (< 300 ppb) in the Ni-laterite profiles of the Oman ophiolite do not reach the economic values, they are mostly comparable to the total PGE contents reported from PGE-rich Ni-laterite profiles around the world, such as Ni-laterite deposits of Falcondo in the Dominican Republic, Cuba (Aiglsperger et al., 2015, 2016), and New Caledonia (Traoré et al., 2008); Ni-laterite from Centinela Bajo, south-central Chile (Rivera et al., 2018); and those from the Cerro Matoso and Planeta Rica Ni-Laterite deposits, Northern Colombia (Tobón et al., 2020). For example, the Ni-laterite deposit of Falcondo of the Dominican Republic has PGE values before processing between 250 and 640 ppb. However, the final product obtained after

pyrometallurgical extraction shows an increase in total PGE contents up to 2 ppm (Aiglsperger et al., 2015, 2016). Similarly, in the Ni-laterite deposits of Cuba, the PGMs are mainly collected in the sulfide concentrates and the Ni-end products during the ore dressing in the Nikaro and Moa ore dressing plants, where the PGE contents reach up to 6 ppm (Lazarenkov et al., 2005). Such final PGE values are considered as a potential unconventional PGE resource from the Falcondo and Cuba Ni-laterite deposits.

In the Ni-laterite profiles of the Oman ophiolite, the PGE contents in the oxide/clay-rich zone reach up to 253 ppb (up to 6 magnitude as those in the parent ultramafic rocks), which is almost comparable to those reported from worldwide PGE-rich Ni-laterite deposits (Figure 12). The PGE enrichment in the oxide zone of the laterite profiles corresponds to an increase in NiO, Co_3O_4, Cr_2O_3, Fe_2O_3, and Al_2O_3 contents, as well as to the highest calculated degrees of lateritization (average UMIA ~70%) (Figures 11a–d). The formation of secondary nanoparticles of PGE alloys in the oxide and oxyhydroxide zones of the Oman laterite profiles needs more careful investigation using ultrahigh magnification tools such as the field emission scanning electron microscope (FESEM) and/or Raman spectroscopy techniques, which is beyond the scope of this article. In addition, further field investigations and systematic sampling are needed to focus on the profiles having more concentration of Cr_2O_3 contents and progressive high degrees of lateritization. Although the PGE contents in the oxidized horizons of the Oman Ni-laterite profiles are not economic in its current natural form, applying adequate extraction and refining methods in the future could increase the PGE contents, which might be recovered as by-products. If it is applied in the future, the Ni laterite of the Oman ophiolite can be considered as unconventional PGE deposits.

6. Conclusions

1. The Ni-laterite profiles of the Oman ophiolite characterized by the progressive increase in Fe_2O_3 Al_2O_3, Cr_2O_3, NiO, and Co_3O_4 concentrations from parent ultramafic rocks to the oxide/clay-rich zone in the uppermost part of the laterite profile. This also corresponds to the strong leaching of SiO_2 and MgO contents from the oxidized zone of the laterite profiles.
2. The highest PGE contents in the Ni-laterite of the Oman ophiolite are concentrated in the oxide/clay-rich zone, which reached up to six times as their concentration in the saprolite and unweathered peridotite protolith. The PGE distribution patterns and their positive correlation

with the UMIA, as well as the Cr_2O_3 contents in the laterite profiles, indicate that the PGE can be mobilized in different proportions.

3. Ru, Pt, and Pd are more mobile than Os, Ir, and Rh. Osmium, by far, is the less-resistant PGE metal under the surficial weathering environment. The positive correlation between IPGE and PPGE with the increasing degree of lateritization is indicative of their mobilization, redistribution, and enrichment in the Fe-rich oxides and oxyhydroxides of the laterite profiles. The IPGE are most probably linked with the residual accumulation of chromite in the oxide zone, while the PPGE are most probably leached from the interstitial sulfides and co-precipitated as nanoparticles of PGE alloys with the Fe oxide and oxyhydroxide materials.
4. The PGE contents of the Oman Ni-laterite are in accordance with the PGE values from the worldwide Ni-laterite deposits. It can be considered as an unconventional PGE resource if adequate extraction and refining processes are applied to increase the PGE contents in the final products.
5. Further field investigations focusing on the Ni-laterite profiles with high degrees of lateritization and those enriched in Cr_2O_3 contents are needed to check the existence of PGE enrichment in these laterite profiles. A detailed mineralogical study using ultrahigh magnification tools is also needed to identify the possible presence of PGE-Fe alloy nanoparticles in the oxide and oxyhydroxide zones of the Ni-laterites.

Acknowledgments

This research was funded by the SQU Deanship of Research (RF/SCI/ETHS/20/01). We appreciate the Department of Earth Sciences and the Central Analytical Applied Research Unit (CAARU) for allowing us to use their analytical facilities. Dataset supports this research is from Al-Khirbash, S.A. (2016). Geology, mineralogy, and geochemistry of low grade Ni-lateritic soil (Oman Mountains, Oman). *Chemie der Erde, 76(3),* 363–381. https://doi.org/10.1016/j.chemer.2016.08.002.

The authors declare that there is no conflict of interest.

References

462 Abbasi, I.A., Salad Hersi, O., & Al-Harthy A. (2014). Late Cretaceous post-obduction
463 conglomerates of the Qahlah Formation, north Oman: Depositional system and implications
464 for basin configuration. In: H.R Rollinson., M.P. Searle, I.A. Abbasi, A. Al-Lazki, & M.H.
465 Al Kindi (eds.). Tectonic Evolution of the Oman Mountains: *Geol. Soc. Spec. Publ., 392(1),*
466 325–341. DOI: 10.1144/SP392.17
467 Ahmed, A., & Arai, S. (2002). Unexpectedly high-PGE chromitite from the deeper mantle
468 section of the northern Oman ophiolite and its tectonic implications. *Contributions to*
469 *Mineralogy and Petrology, 143***,** 263–278. https://doi.org/10.1007/s00410-002-0347-8.
470 Ahmed, A., & Arai, S. (2003). Platinum-group minerals in podiform chromitities of the Oman
471 ophiolite. *The Canadian Mineralogist, 41 (3),* 597–
472 616.doi: https://doi.org/10.2113/gscanmin.41.3.597.
473 Ahmed, A.H., Arai, S. & Kadoshima, K. (2002). Possible platinum-group element (PGE) oxides
474 in the PGE-mineralized chromitite from the northern Oman ophiolite. *Journal of*
475 *Mineralogical and Petrological Sciences, 97*, 190-198. https://doi.org/10.2465/jmps.97.190
476 Aiglsperger, T., Proenza, J.A., Zaccarini, F., Lewis, J.F., Garuti, G., Labrador, M., & Longo,
477 F. (2015). Platinum group minerals (PGM) in the Falcondo Ni laterite deposit, Loma Caribe
478 peridotite (Dominican Republic). *Mineralium Deposita, 50*, 105-123.
479 https://doi.org/10.1007/s00126-014-0520-
480 Aiglsperger, T., Proenza, J.A., Lewis, J.F., Labrador, M., Svojtka, M., Rojas-Purón, A.,
481 Longo, F. & Ďurišová, J. (2016). Critical metals (REE, Sc, PGE) in Ni laterites from Cuba
482 and the Dominican Republic. *Ore Geology Review, 73*, 127-147.
483 https://doi.org/10.1016/j.oregeorev.2015.10.010
484 Aiglsperger, T., Proenza, JA., Font-Bardia, M, Baurier-Aymat, S., Galí, S., Lewis, J.F., &
485 Longo, F. (2017). Supergene neoformation of Pt-Ir-Fe-Ni alloys: multistage grains explain
486 nugget formation in Ni-laterites. *Mineralium Deposita, 52*, 1069–1083.
487 https://doi.org/10.1007/s00126-016-0692-6.
488 Al-Khirbash, S., Nasir, S., Al-Harthy, A., Richard, L., Al-Sayigh, A., Darkel, A., & Semhi, K.
489 (2010). Geology and Ni-Co mineralization of laterites of the Oman Mountains, 7th
490 International Symposium on the Eastern Mediterranean Geology, 18–22 October. Cukurova
491 University, Adana.

Al-Khirbash, S. (2015). Genesis and Mineralogical Classification of Ni-laterites, Oman Mountains. *Ore Geology Reviews, 65,* 199–212. https://doi.org/10.1016/j.oregeorev.2014.09.022

Al-Khirbash, S.A. (2016). Geology, mineralogy, and geochemistry of low grade Ni-lateritic soil (Oman Mountains, Oman). *Chemie der Erde, 76(3),* 363–381. https://doi.org/10.1016/j.chemer.2016.08.002

Al-Khirbash, S. (2020). Mineralogical characterization of low-grade nickel laterites from the North Oman Mountains: Using mineral liberation analyses – scanning electron microscopy-based automated quantitative mineralogy. *Ore Geology Review, 120*. https://doi.org/10.1016/j.oregeorev.2020.103429

Al-Khirbash, S., Semhi, K., Richard, L., Nasir, S., & Al-Harthy, A.R. (2014). Rare earth element mobility during laterization of the mafic rocks of the Oman Mountains. *Arab Journal Geoscience, 7,* 5443-5454. 10.1007/s12517-013-1189-6.

Augé, T., & Legendre, O. (1994). Platinum-group element oxides form the pirogues ophiolitic mineralization, New Caledonia: Origin and significance. *Economic Geology, 89,* 1454-1468. https://doi.org/10.2113/gsecongeo.89.7.1454

Babechuk, M.G., Kamber, B.S., & Widdowson, M. (2014). Quantifying chemical weathering intensity and trace element release from two contrasting basalt profiles, Deccan Traps, India. *Chemical Geology, 363,* 56-75. https://doi.org/10.1016/j.chemgeo.2013.10.027

Bandyayera, D. (1997). Formation de laterites nickeliferes et mode de distribution des elements du groupe du platine dans les profils lateritiques du complexe de Musongati, Burundi (Ph.D. Thesis). Universite du Quebec a Chicoutimi, 440 pp. 10.1522/1531842

Barnes, S.J., Naldrett, A.J., & Gorton, M.P. (1985). The origin of the fractionation of platinum-group elements in terrestrial magmas. *Chemical Geology, 53,* 3O3-323. https://doi.org/10.1016/0009-2541(85)90076-2

Barnes, S.J., Boyd, R., Korneliussen, A., Nilsson, L.P., Often, M., Pedersen, R.B., & Robins, B. (1988). The use of mantle normalization and metal ratios in discriminating between the effects of partial melting, crustal fractionation and sulphide segregation on platinum group elements, gold, nickel and copper: Examples from Norway. In H.M. Prichard, P.J. Potts, J.F.W. Bowles, & S.J. Cribbs (eds.). *Geoplatinum-87: London, Elsevier, Applied Science*, pp. 113–143.

Bowles, J.F.W., Gize, A.P., & Cowden, A. (1994a). The mobility of the Platinum-Group elements in the soils of the Freetown peninsula, Sierra Leone. *Canadian Mineralogist, 32*, 957-967.

Bowles, J.F.W., Gize, A.P., Vaughan, D.J., & Norris, S.J. (1994b). The development of Platinum-Group Minerals in latérites; inorganic and organic controls. Transactions of the Institution of Mining and Metallurgy, Section B: *Applied Earth Science, 103*, 53-56

Bowles, J.F.W., Suárez, S., Prichard, H.M., & Fisher, P.C. (2017). Weathering of PGE sulfides and Pt–Fe alloys in the Freetown Layered Complex, Sierra Leone. *Minerlium Deposita, 52***,** 1127–1144. https://doi.org/10.1007/s00126-016-0706-4

Butt, C., & Cluzel, D. (2013). Nickel Laterite Ore Deposits: Weathered Serpentinites. *Elements, 9(2),* 123-128. https://doi.org/10.2113/gselements.9.2.123

Cabral, A.R., Lehmann, B., Tupinambá, M., Schlosser, S., Kwitko-Ribeiro, R., & De Abreu, F.R. (2009). The platiniferous Au-Pd belt of Minas Gerais, Brazil, and genesis of its botryoidal Pt-Pd aggregates. *Economic Geology, 104(8),* 1265–1276. https://doi.org/10.2113/gsecongeo.104.8.1265

Cabral, A.R., Radtke, M., Munnik, F., Lehmann, B., Reinholz, U., Riesemeier, H., Tupinambá, M., & Kwitko-Ribeiro, R. (2011). Iodine in alluvial platinum-palladium nuggets: evidence for biogenic precious-metal fixation. *Chemical Geology, 281(1-2),* 152–132. https://doi.org/10.1016/j.chemgeo.2010.12.003

Colombo, C., Oated, C.J., Monhemius, A.J., & Plant, J.A. (2008). Complexation of platinum, palladium and rhodium with inorganic ligands in the environment. *Geochemistry: Exploration, Environment, Analysis, 8*, 91–101. https://doi.org/10.1144/1467-7873/07-151

Cornelius, M., Robertson, I.D.M., Cornelius, A.J., & Morris, P.A. (2008). Geochemical mapping of the deeply weathered western Yilgarn craton of Western Australia using laterite geochemistry. *Geochemistry: Exploration, Environment, Analysis, 8(3-4),* 241-254. https://doi.org/10.1144/1467-7873/08-172

Cowan, R. J., Searle, M. P., & Waters, D. J. (2014). Structure of the metamorphic sole to the Oman Ophiolite, Sumeini Window and Wadi Tayyin: implications for ophiolite obduction processes. *Geological Society, London, Special Publications, 392*, 155-175. https://doi.org/10.1144/SP392.8

553 Duzgoren-Aydin, N.S., Aydin, A., & Malpas, J. (2002). Distribution of clay minerals along a
554 weathered pyroclastic rock profile, Hong Kong. *Catena, 50(1),* 17-41.
555 https://doi.org/10.1016/S0341-8162(02)00066-8
556 Edwards, S.J. (1990). Harzburgites and refractory melts in the Lewis Hills massif, Bay of Island
557 ophiolite complex: the base-metals and precious-metals story. *Canadian Mineralogist, 28,*
558 537–552
559 Eliopoulos, D.G., & Economou-Eliopoulos, M. (2000). Geochemical and mineralogical
560 characteristics of Fe–Ni- and bauxitic-laterite deposits of Greece. *Ore Geology Reviews,*
561 *16(1-2),* 41–58. https://doi.org/10.1016/S0169-1368(00)00003-2
562 Freyssinet, P., Butt, C.R.M., Morris, R.C., & Piantone, P. (2005). Ore-forming processes related
563 to lateritic weathering. In J.W. Hedenquist, J. F. H. Thomson, R. J. Goldfarb, & J. P.
564 Richards (eds.). *Economic Geology 100th Anniversary Volume*.
565 https://doi.org/10.5382/AV100.21
566 Garuti, G., Zaccarini, F., Moloshag, V., & Alimov, V. (1999). Platinum-group minerals as
567 indications of sulfur fugacity in ophiolitic upper mantle: an example from chromitites of the
568 Ray-is ultramafic complex, Polar Urals, Russia. *Canadian Mineralogist, 37(5),* 1099-1115.
569 Garuti, G., Proenza, J.A., & Zaccarini, F. (2007). Distribution and mineralogy of platinum-group
570 elements in altered chromitites of the Campo Formoso layered intrusion (Bahia State,
571 Brazil): control by magmatic and hydrothermal processes. *Mineralogy and Petrology, 89,*
572 159–188.10.1007/s00710-006-0141-9
573 Garuti, G., Zaccarini, F., Proenza, J.A., Thalhammer, O.A.R., & Angeli, N. (2012). Platinum-
574 group minerals in chromitites of the Niquelândia layered intrusion (Central Goias, Brazil):
575 their magmatic origin and low-temperature reworking during serpentinization and lateritic
576 weathering. *Minerals, 2(4),* 365–384. https://doi.org/10.3390/min2040365
577 Golightly, J.P. (1981). Nickeliferous laterite deposits. *Economic Geology 75th Anniversary*
578 *Volume,* 710–735.
579 Golightly, J.P. (2010). Progress in understanding the evolution of nickel laterites, *Society of*
580 *Economic Geology, Special Publication, 15*, 451−486. https://doi.org/10.5382/SP.15.2.07
581 Gray, J.D., Schorin, K.H., & Butt, C.R.M. (1996). Mineral associations of platinum and
582 palladium in lateritic regolith, Ora Banda Sill, Western Australia. *Journal of Geochemical*
583 *Exploration, 57(1-3),* 245-255. https://doi.org/10.1016/S0375-6742(96)00040-4

584 Keays, R.R., Ross, J.R., & Woolrich, P. (1981). Precious metal sin volcanic peridotite-associated
585 nickel sulfide deposits in Western Australia. II. Distribution within the ores and host rocks at
586 Kambalda. *Economic Geology, 76,* 1645–1674.
587 Keays, R.R., Nickel, E.H., Groves, D.I., & McGoldrick, P.J. (1982). Iridium and palladium as
588 discriminants of volcanic-exhalative hydrothermal and magmatic nickel sulfide
589 mineralization. *Economic Geology, 77(6),* 1535–1547.
590 https://doi.org/10.2113/gsecongeo.77.6.1535
591 Lazarenkov, V.G., Tikhomirov, B., Zhidkov, Y., & Talovina, V. (2005). Platinum group metals
592 and gold in supergene nickel ores of the Moa and Nikaro deposits (Cuba). *Lithology and*
593 *Mineral Resources, 40,* 521-527. https://doi.org/10.1007/s10987-005-0049-1
594 Maier, W.D., Barnes, S-J., Chinyepi, G., Barton, Jr.J.M., Eglington, B., & Setshedi, I. (2008).
595 The composition of magmatic Ni–Cu–(PGE) sulfide deposits in the Tati and Selebi-Phikwe
596 belts of eastern Botswana. *Minerlium Deposita, 43,* 37–60. I 10.1007/s00126-007-0143-5
597 Mattern, F., Scharf, A., Pu-Jun Wang, P.J., Callegari, I., Abbasi, A., Al-Wahaibi, S., Pracejus,
598 B., & Scharf, K. (2020). Deformation of the Cambro-Ordovician Amdeh Formation
599 (Members 1 and 2): Characteristics, Origins, and Stratigraphic Significance (Wadi Amdeh,
600 Saih Hatat Dome, Oman Mountains). *Geosciences, 10 (2),*
601 *48.* https://doi.org/10.3390/geosciences10020048.
602 Ndjigui, P.D., & Bilong, P. (2010). Platinum-group elements in the serpentinite lateritic mantles
603 of the Kongo–Nkamouna ultramafic massif (Lomié region, South-East Cameroon). *Journal*
604 *of Geochemical Exploration,107(1),* 63-76. 10.1016/j.gexplo.2010.06.008.
605 Oberthür, T., & Melcher, F. (2005). PGE and PGM in the supergene environment: The Great
606 Dyke, Zimbabwe, In J.E. Mungall (ed.), Exploration for platinum-group element deposits.
607 Mineralogical Association of Canada, *Short Course Series, 35,* 97-112.
608 Plimer, I.R., & Willians, P.A. (1988). New mechanism for the mobilization of the Platinum
609 Group Elements in the supergene zone. In H. M. Prichard, P. J. Potts, J. F. W. Bowles, S.
610 J. Cribb (eds.), Geo-Platinum 87, *Elsevier Applied Science Publications, London, U.K.,*
611 pp. 83–92. https://doi.org/10.1007/978-94-009-1353-0_9
612 Prichard, H.M., Lord, R.A., & Neary, C.R. (1996a). A model to explain the occurrence of
613 platinum- and palladium-rich ophiolite complexes. London: *Journal of Geological*
614 *Society, 153,* 323-328. https://doi.org/10.1144/gsjgs.153.2.0323

615 Prichard, H.M., Puchelt, H., Eckhardt, J-D., & Fisher, P.C. (1996b). Platinum-group element
616 concentrations in mafic and ultramafic lithologies drilling from Hess Deep. In C. Me´vel,
617 K. M. Gillis, J. F. Allan, & P. S. Meyer (eds.), *Proceedings of Ocean Drilling Program,*
618 *Scientific Results, 147*, pp 77–90. 10.2973/odp.proc.sr.147.004.1996
619 Proenza, J.A., Zaccarini, F., Lewis, J., Longo, F., & Garuti, G. (2007). Chromian spinel
620 composition and platinum-group mineral assemblage of PGE-rich Loma Peguera
621 chromitites, Loma Caribe peridotite, Dominican Republic. *Canadian Mineralogist, 45,* 211-
622 228.
623 Proenza, J.A., Roqué, J., Labrador, M., Galí, S., Tauler, E., Gallardo, T., Lewis, J. F., & Longo,
624 F. (2010). Mineralogical composition and mineral chemistry of supergene cobalt ores from
625 eastern Cuba and Dominican Republic Ni-laterite deposits, *20th general meeting of the IMA,*
626 21-27.
627 Reich, M., & Vasconcelos, P. (2015). Geological and economic significance of supergene
628 upgrading of metals. *Elements, 11(5),* 305-310. https://doi.org/10.2113/gselements.11.5.305
629 Rivera, J., Reich, M., Schoenberg, R., González-Jiménez, J.M., Barra, F., Aiglsperger, T.,
630 Proenza, J.A., & Carretier, S. (2018). Platinum-group element and gold enrichment in soils
631 monitored by chromium stable isotopes during weathering of ultramafic rocks. *Chemical*
632 *Geology, 499,* 84-99. https://doi.org/10.1016/j.chemgeo.2018.09.008
633 Roberts, S. (1986). The role of igneous processes in the formation of ophiolitic chromitite (Ph.D.
634 Thesis). Open University, Milton Keynes.
635 https://ethos.bl.uk/OrderDetails.do?uin=uk.bl.ethos.374493
636 Salpéteur, I., Martel-Jantin, B., & Rakotomanana, D. (1995). Pt and Pd mobility in ferrallitic
637 soils of the West Andriamena area (Madagascar). Evidence of a supergene origin of some Pt
638 and Pd minerals. *Chronicle of mineral research and exploration, 520,* 27-45.
639 Searle, M.P., & Cox, J. (2002). Subduction zone metamorphism during formation and
640 emplacement of the Semail ophiolite in the Oman Mountains. *Geological Magazine, 139(3),*
641 241-255. https://doi.org/10.1017/S0016756802006532
642 Searle M.P. (2019). Ophiolites and Regional Tectonics. In: Geology of the Oman
643 Mountains, Eastern Arabia. GeoGuide. Springer, Cham. https://doi.org/10.1007/978-3-
644 030-18453-7_4

Stockman, H.W., & Hlava, P.F. (1984). Platinum-group minerals in Alpine chromitites from southwestern Oregon. *Economic Geology, 79(3),* 491-508. https://doi.org/10.2113/gsecongeo.79.3.491

Stumpfl, E.F. (1986). Distribution, transport and concentration of platinum-group elements. In M. J. Gallagher, R. A. Ixer, C. R. Neary, & H. M. Prichard (eds.), Metallogeny of basic and ultrabasic rocks. Institute of Mining and Metallurgy Publications, London, pp 379–394. http://pascal-francis.inist.fr/vibad/index.php?action=getRecordDetail&idt=8819820

Talovina, I.V., & Lazarenkov, V.G. (2001). Distribution and genesis of platinum group minerals in nickel ores of the Sakhara and Elizavet deposits in the Urals. *Lithology and Mineral Resources, 36,* 116–122. https://doi.org/10.1023/A:1004870316406

Thorne, R., Roberts, S., & Herrington, R. (2012a). The formation and evolution of the Bitincke nickel laterite deposit, Albania. *Mineralium Deposita, 47(8),* 933–947. http://dx.doi.org/10.1007/s00126-012-0411-x

Thorne, R.L., Roberts, S., & Herrington, R. (2012b). Climate change and the formation of nickel laterite deposits. *Geology, 40(4),* 331–334. https://doi.org/10.1130/G32549.1

Traoré, D., Beauvais, A., Chabaux, F., Peiffert, C., Parisot, J.C., Ambrosi, J.P., & Colin, F. (2008). Chemical and physical transfers in an ultramafic rock weathering profile: part 1. Supergene dissolution of Pt-bearing chromite. *American Mineralogist, 93(1),* 22–30. https://doi.org/10.2138/am.2008.2605

Tobón, M., Weber, M., Proenza, J.A., Aiglsperger, T., Betancur, S., Farré-de-Pablo, J., Ramírez, C., & Pujol-Solà, N. (2020). Geochemistry of platinum-group elements (PGE) in Cerro Matoso and Planeta Rica Ni-laterite deposits, northern Colombia. Boletín de la Sociedad *Geológica Mexicana, 72(3),* A201219. http://dx.doi.org/10.18268/ BSGM2020v72n3a201219

Tupaz, C.A.J., Watanabe, Y., Sanematsu, K., Echigo, T., Arcilla, C., & Ferrer, C. (2020). Ni-Co Mineralization in the Intex Laterite Deposit, Mindoro, Philippines. *Minerals, 10(7),* 579. https://doi.org/10.3390/min10070579

Varajão, C.A.C., Colin, F., Vieillard, P., Melfi, A.J., & Nahon, D. (2000). Early weathering of palladium gold under lateritic conditions, Maquiné mine, Minas Gerais, Brazil. *Applied Geochemistry, 15(2),* 245–263. https://doi.org/10.1016/S0883-2927(99)00038-4

Zaccarini, F., Proenza, A.J., Ortega-Gutierrez, F., & Garuti, G. (2005). Platinum group minerals in ophiolitic chromitites from Tehuitzingo (Acatlan complex, southern Mexico): implications for post-magmatic modification. *Mineralogy and Petrology, 84*, 147-168. 10.1007/s00710-005-0075-7

Zaccarini, F., Proenza, J.A., Rudashevsky, N.S., Cabri, L.J., Garuti, G., Rudashevsky, V.N., Melgarejo, J.C., Lewis, J.F., Longo, F., Bakker, R., & Stanley, C.J. (2009). The Loma Peguera ophiolitic chromitite (Central Dominican Republic): a source of new platinum group minerals (PGM) species. *Neues Jahrbuch für Mineralogie Abhandlungen, Journal of Mineralogy and Geochemistry, 185(3),* 335-349. https://doi.org/10.1127/0077-7757/2009/0127

List of Figures

Figure 1. (a) Geological map of the Oman Mountains and the location of the study area (modified after Mattern et al., 2020). (b) Geological map of the studied area with the studied sections (modified after Al-Khirbash, 2015).

Figure 2: Lithological sections of the six studied laterites (localities 1–6) (modified after Al-Khirbash, 2015).

Figure 3: Field photographs of the laterite horizons in the study area: (a) massive layered gabbro protolith, locality #3; (b) general view of the peridotite protolith, locality #5; (c) saprolite horizon with less altered peridotite blocks, locality #4; (d) massive oxide horizon, locality #6; and (e) pisolitic reddish color oxide horizon, locality #6.

Figure 4: Photomicrographs of the protolith and laterite horizons: (a) fresh plagioclase (Pl) crystals and altered pyroxenes (Cpy) in layered gabbro, XPL, locality #3; (b) pyroxene (Cpy) crystals that are altered to lizardite (lz) and chrysotile (Ctl) in serpentinized peridotites, XPL, locality #2; (c) lizardite (lz) and chrysotile (Ctl) minerals cut by carbonate-filling (Cb) fracture in

706 the saprolite horizon, XPL, locality #3; (d) hematite and goethite minerals with rounded chlorite-
707 core (Chl) pisolites in the oxide horizon, XPL, locality #4; and (e) hematite (Hem) and goethite
708 (Gth), with magnetite (Mag) and inherited chromite (Chr) grains and authigenic chlorite (Chl),
709 reflected XPL, locality #1.
710
711 **Figure 5:** XRD pattern of the representative sample of some selected laterite horizons: (a)
712 saprolite zone, locality # 2; (b) saprolite zone, locality #4; (c) oxide zone, locality #5; and (d)
713 oxide zone, locality # 6. Minerals: Ctl = chrysotile, Nep = nepouite, Lz = lizardite, Cal = calcite,
714 Hem = hematite, Mag = magnetite, Ilm = ilmenite, and Tr = trevorite.
715
716 **Figure 6:** Compositional binary variation diagrams of major oxides of the studied Ni-laterite of
717 the Oman Mountains. a, b, and c are variations of SiO_2 vs. Fe_2O_3, Fe_2O_3, and MgO wt.%, and d is
718 the variation of Fe_2O_3 vs. MgO wt.%.
719
720 **Figure 7:** Compositional variation diagrams of (a) NiO vs. Fe_2O_3 wt.%. b, c, and d are variations
721 of total PGE (ppm) vs. Fe_2O_3, Cr_2O_3, and NiO wt.%, respectively.
722
723 **Figure 8:** (a) Chondrite-normalized PGE distribution diagram of the studied Ni-laterite profiles
724 of the Oman Mountains. (b) Variation diagram of IPGE vs. PPGE of the studied Ni-laterite
725 profiles. Normalizing values are taken from Naldrett and Duke (1980; cf. 514, 540, 690, 200,
726 1,020, and 545 for Os, Ir, Ru, Rh, Pt, and Pd, respectively).
727
728 **Figure 9:** a, b, c, and d are chondrite-normalized PGE distribution patterns of the studied Ni-
729 laterite profiles of the Oman Mountains. Chondrite-normalizing values are taken from Naldrett
730 and Duke (1980).
731
732 **Figure 10:** Ternary plots (in molar %) of Al–Fe–Mg–Si space showing the weathering trends of
733 ultramafic rocks, defined as the ultramafic index of alteration (UMIA): (a) A–SM–F ternary plot
734 illustrating the weathering trend with respect to Al_2O_3 enrichment or Fe_2O_3 enrichment. (b) AF–
735 S–M ternary plot illustrating the general weathering trend of peridotites with the initial loss of
736 MgO, followed by the loss of SiO_2 and concomitant enrichment of Al_2O_3 and Fe_2O_3. Ternary

variation diagrams are from Aiglsperger et al. (2016). (c) Al_2O_3-Fe_2O_3-SiO_2 space shows the index of lateritization (IOL) in wt.% (after Rivera et al., 2018).

Figure 11: (a, b) Variation diagrams of Al_2O_3 vs. Fe_2O_3 wt.% and NiO vs. Co_3O_4 wt.% of the studied Ni-laterite profiles showing the lateritization trend from the protolith to the overlying saprolite and oxidized zones. (c) Variation diagram showing the enrichment of Cr_2O_3 with the increase of the ultramafic index of alteration (UMIA). (d) Variation diagram showing the enrichment of total PGE with the increase of the UMIA.

Figure 12: Chondrite-normalized PGE distribution patterns of the studied Ni-laterite profiles compared with the compositional fields from the Moa Bay and the Falcondo mining areas, including both the pre- and the post-processing materials of PGE concentration. Normalization values from Naldrett and Duke (1980).

List of Tables

Table 1: Major, selected trace elements composition (wt.%) and PGE contents (ppb) of the protolith and saprolite samples of the studied Ni-laterite profiles of the Oman ophiolite.

Table 2: Major, selected trace elements composition (wt.%) and PGE contents of the oxide and clay-rich zone samples of the studied Ni-laterite profiles of the Oman ophiolite.

Figure 1.

(b)

58° 40`

58° 45`

58° 50`

22° 55`

22° 50`

22° 45`

N

5

6

4

3

Saqah

2

Al Niba

1

1: 10 000

(a)

57° E

26° N

Musandam

Iran

United Arab Emirates

Sea of Oman

59° E

Sohar

24° N

Muscat

Oman Mountains

Jabal Akhdar

Saih Hatat

Ibra

Sur

N

100 km

22° N

OBDUCTED

East Oman Ophiolite Complex

Semail Ophiolites

Hawasina

Jurassic to Cretaceous

Permian – Triassic

Precambrian – Palaeozoic

Oman Salt Basins

Crystalline Basement

Thrust front of allochthonous

Wadi sediments

Recent slope sediments

Tertiary carbonates

Laterites

Sheeted dikes

Isotropic gabbro

Layered gabbro

Crustal rocks

Sampled locality

Faults

Uncertain faults

Dunite

Harzburgite

Mantle rocks

Hawasina sediments

Metamorphic sole

Figure 2.

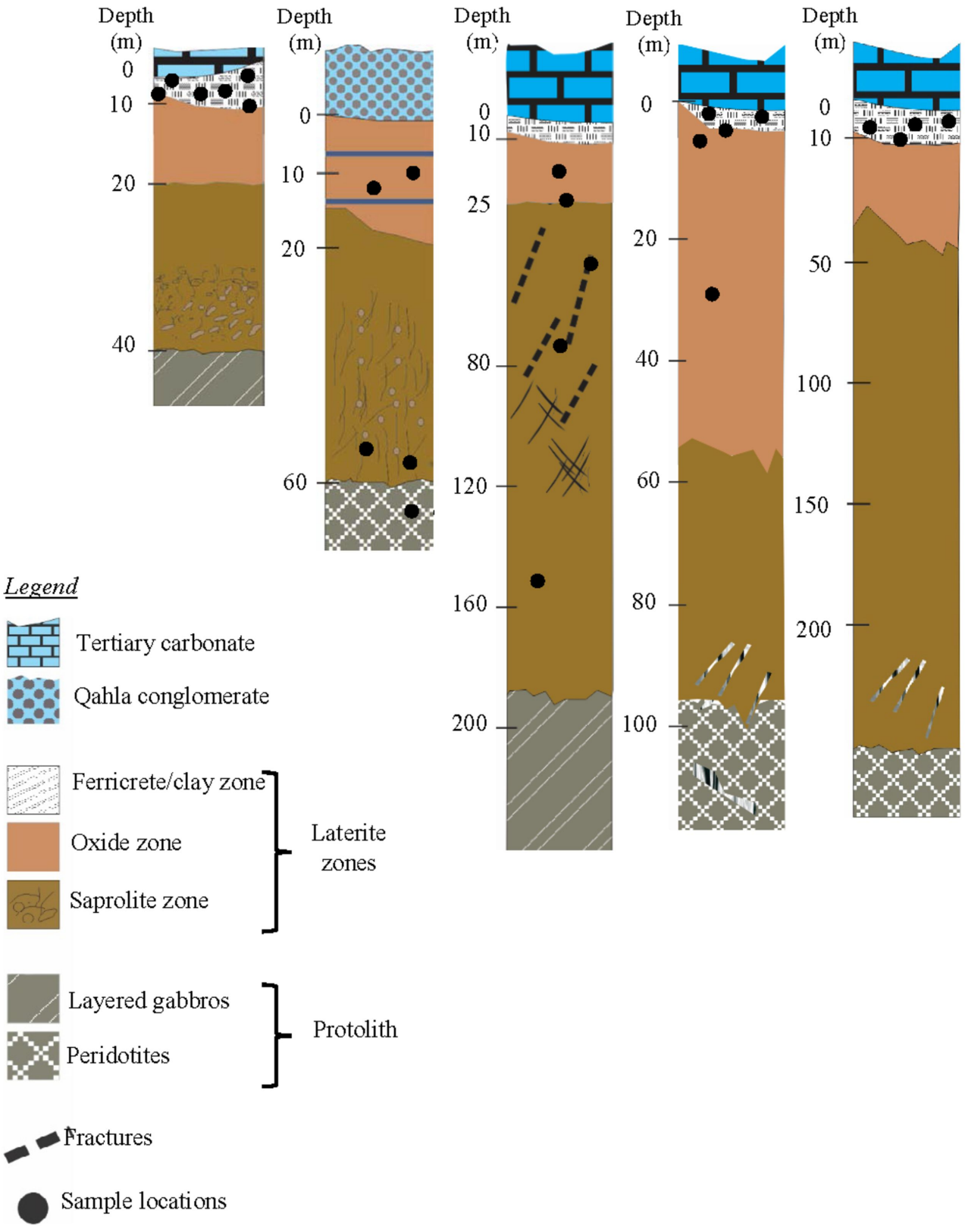
Locality #:
1
2
3 and 4
5
6
Depth (m)
0
10
20
40
Depth (m)
0
10
20
60
Depth (m)
0
10
25
80
120
160
200
Depth (m)
0
20
40
60
80
100
Depth (m)
0
10
50
100
150
200
Legend
Tertiary carbonate
Qahla conglomerate
Ferricrete/clay zone
Oxide zone
Saprolite zone
Laterite zones
Layered gabbros
Peridotites
Protolith
Fractures
Sample locations

Figure 3.

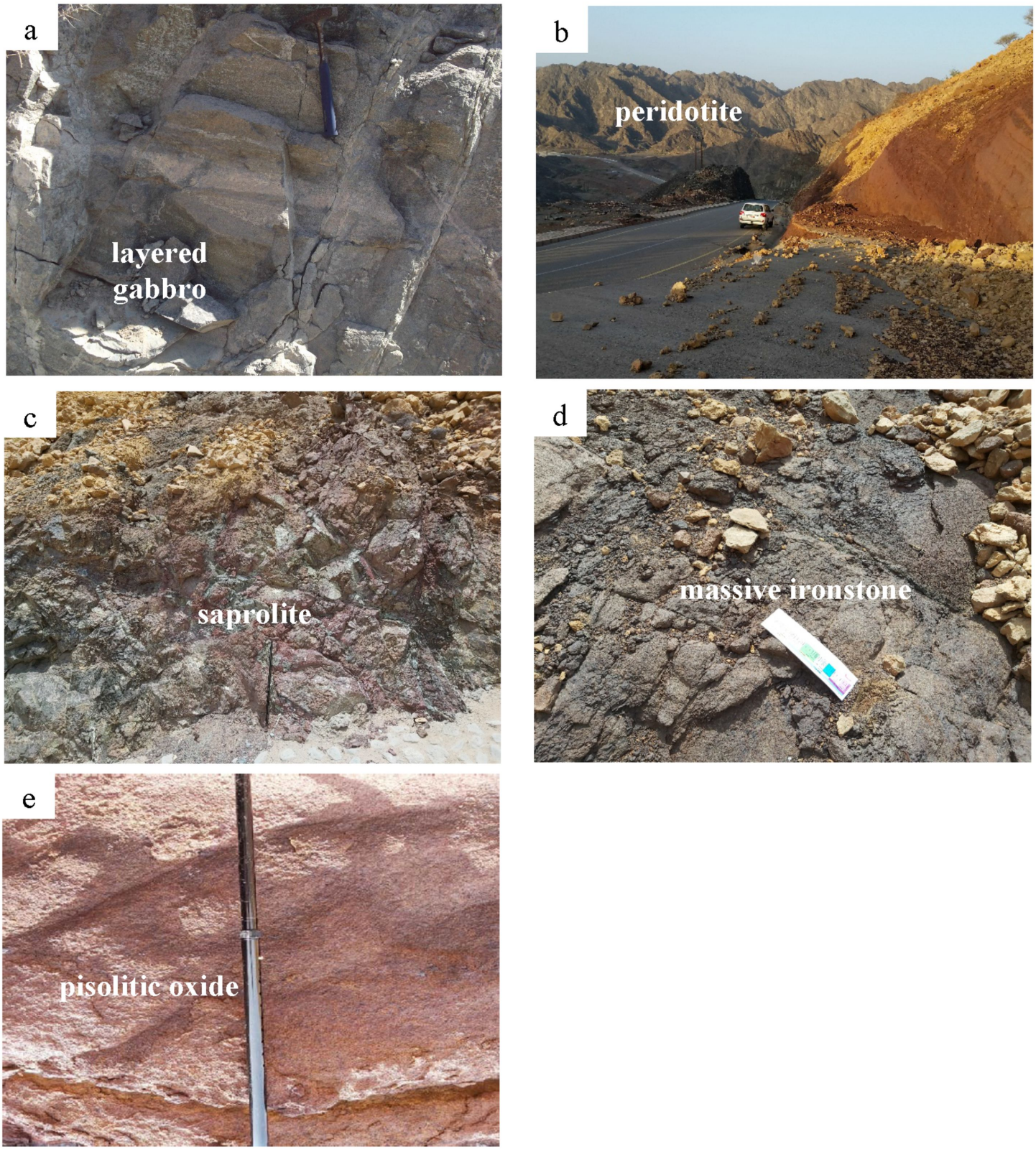
a
layered
gabbro
b
peridotite
c
saprolite
d
massive ironstone
e
pisolitic oxide

Figure 4.

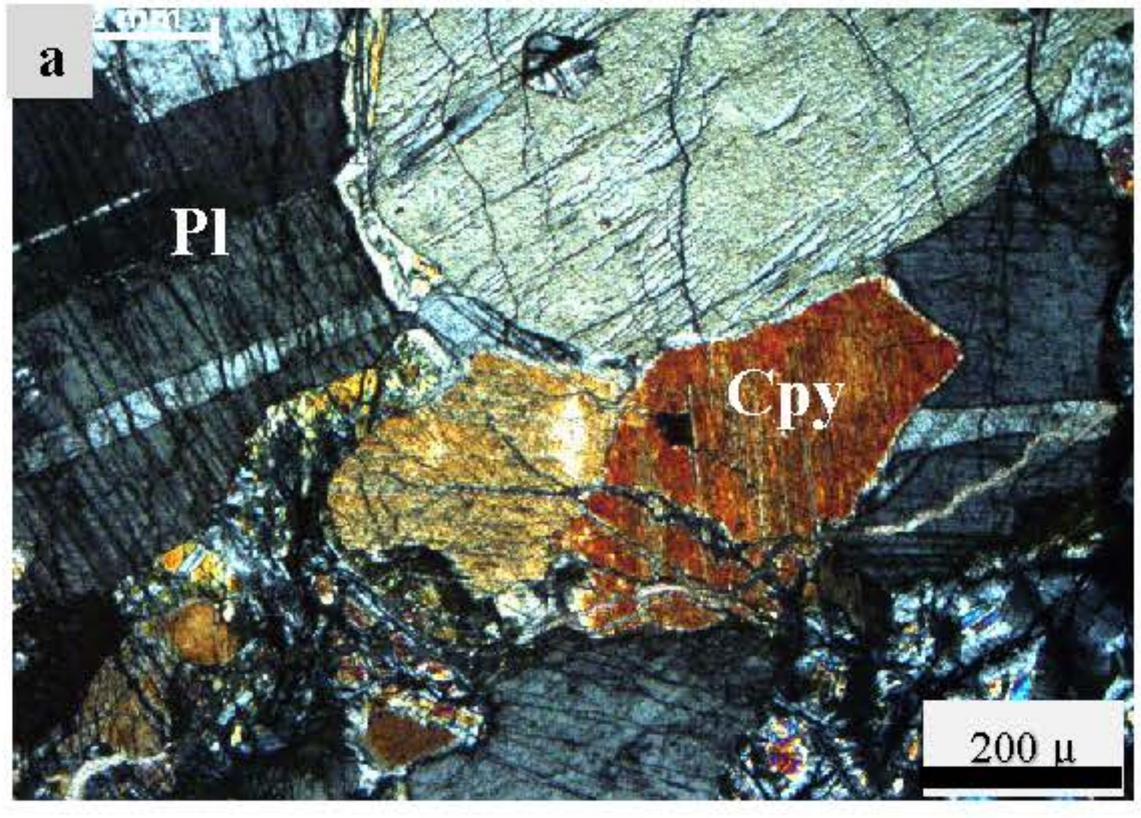
a
Pl
Cpy
200 µ

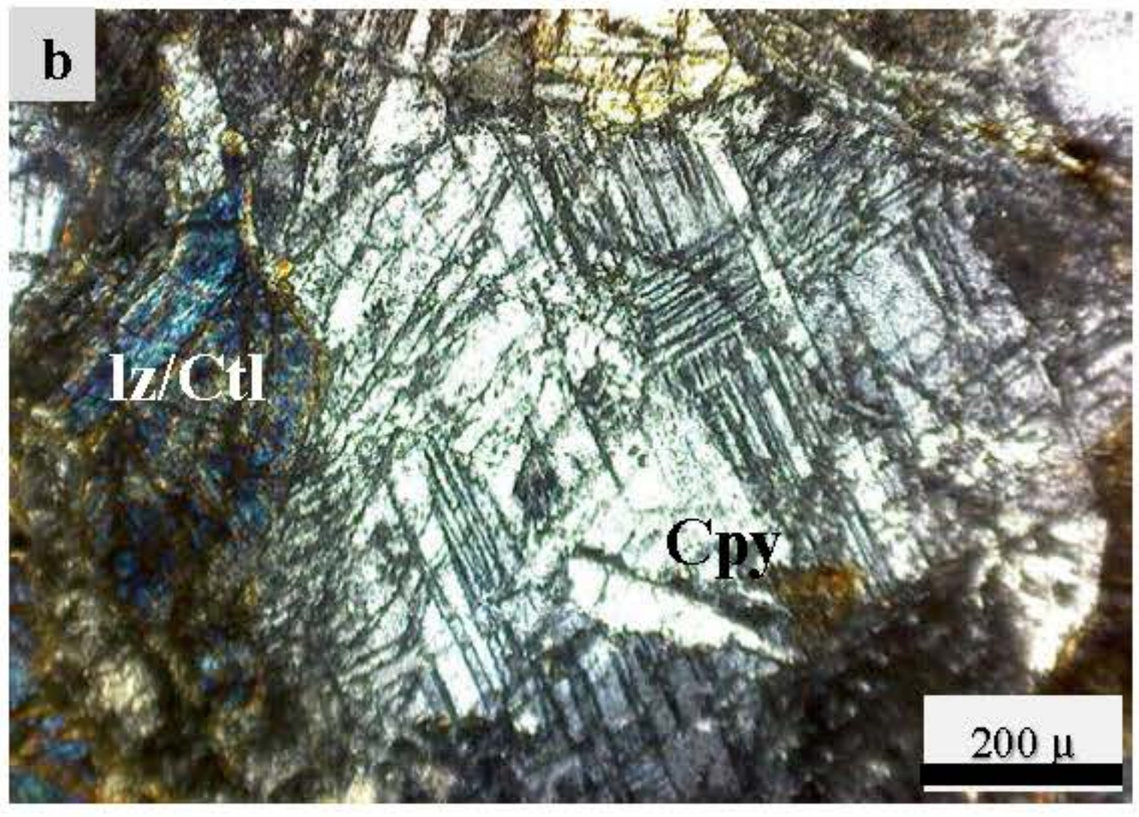
b
Iz/Ctl
Cpy
200 µ

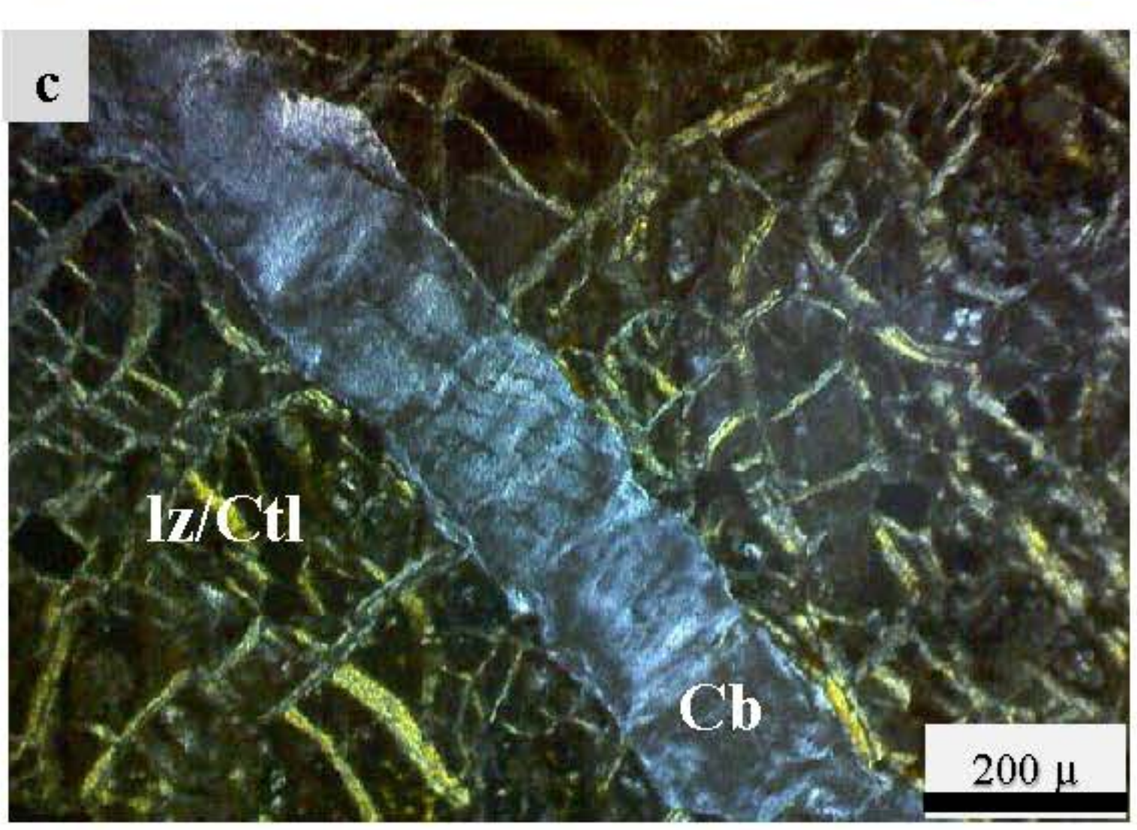
c
Iz/Ctl
Cb
200 µ

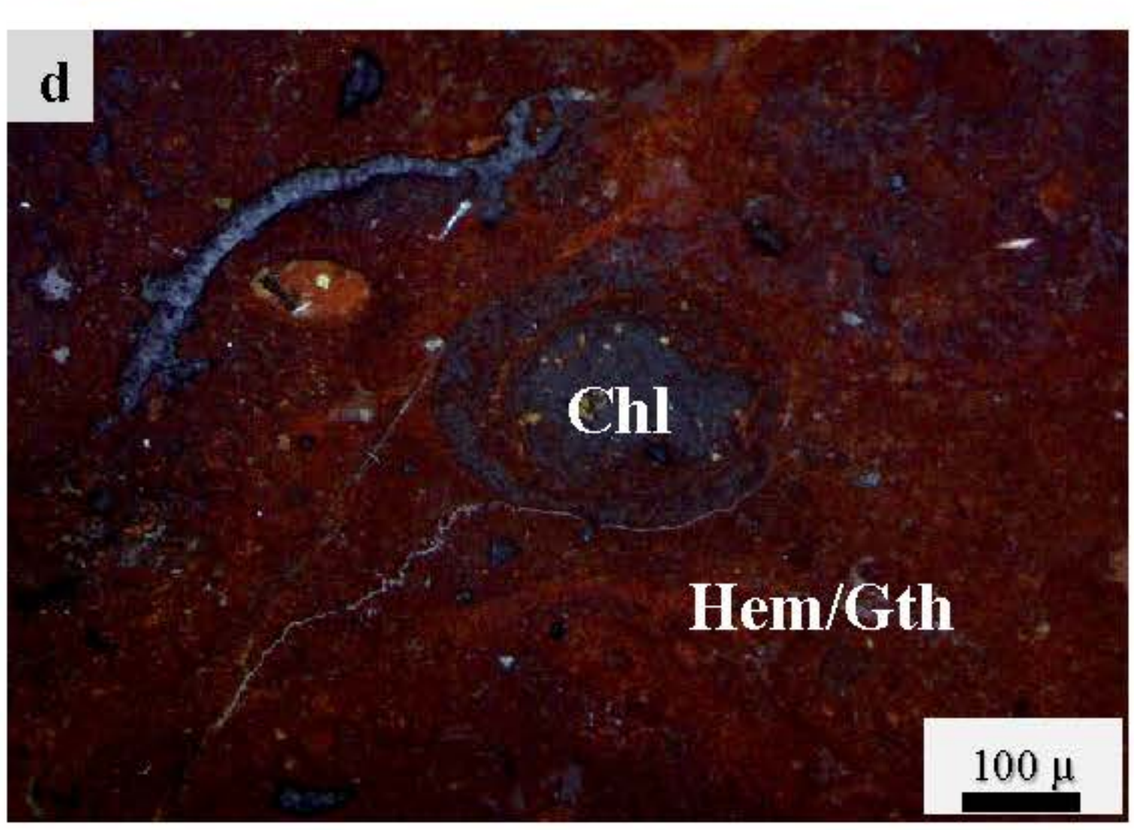
d
Chl
Hem/Gth
100 µ

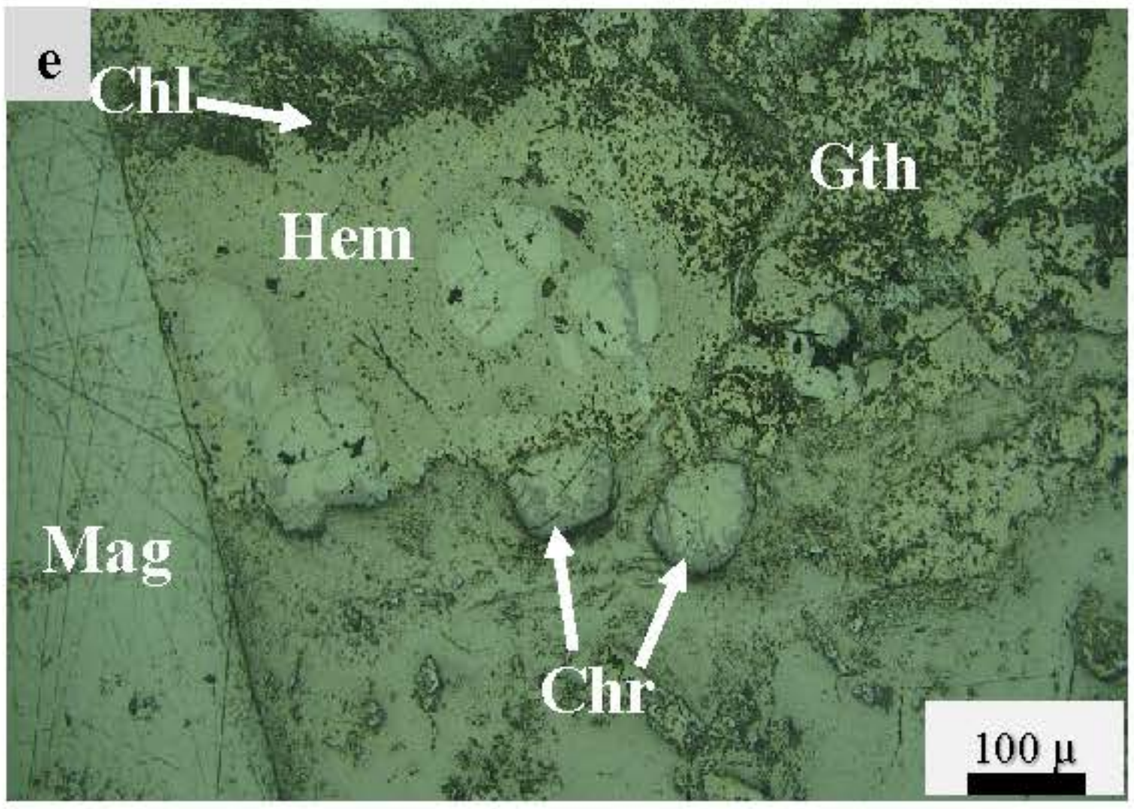
e
Chl
Gth
Hem
Mag
Chr
100 µ

Figure 5.

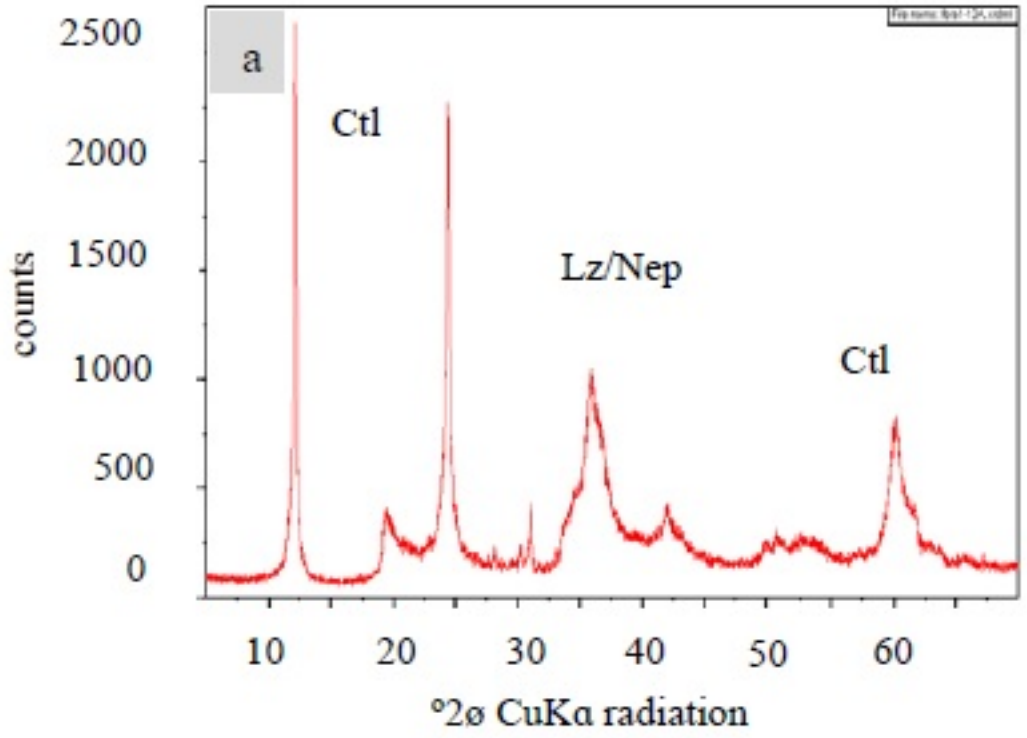
a
Ctl
Lz/Nep
Ctl
counts
°2ø CuKα radiation

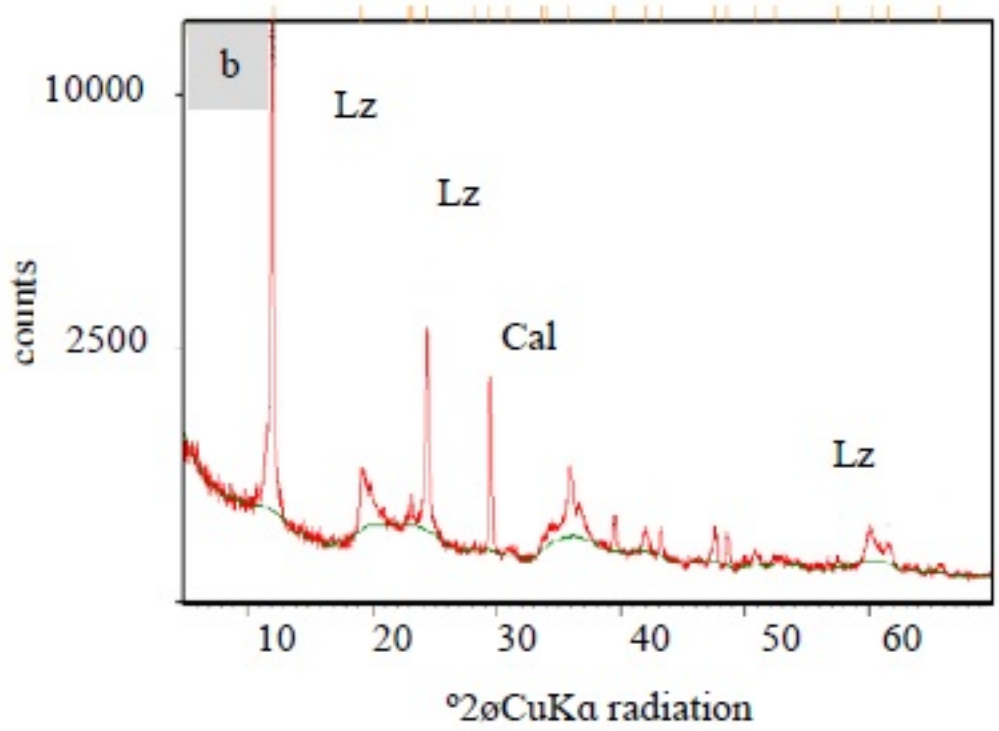
b
Lz
Lz
Cal
Lz
counts
°2øCuKα radiation

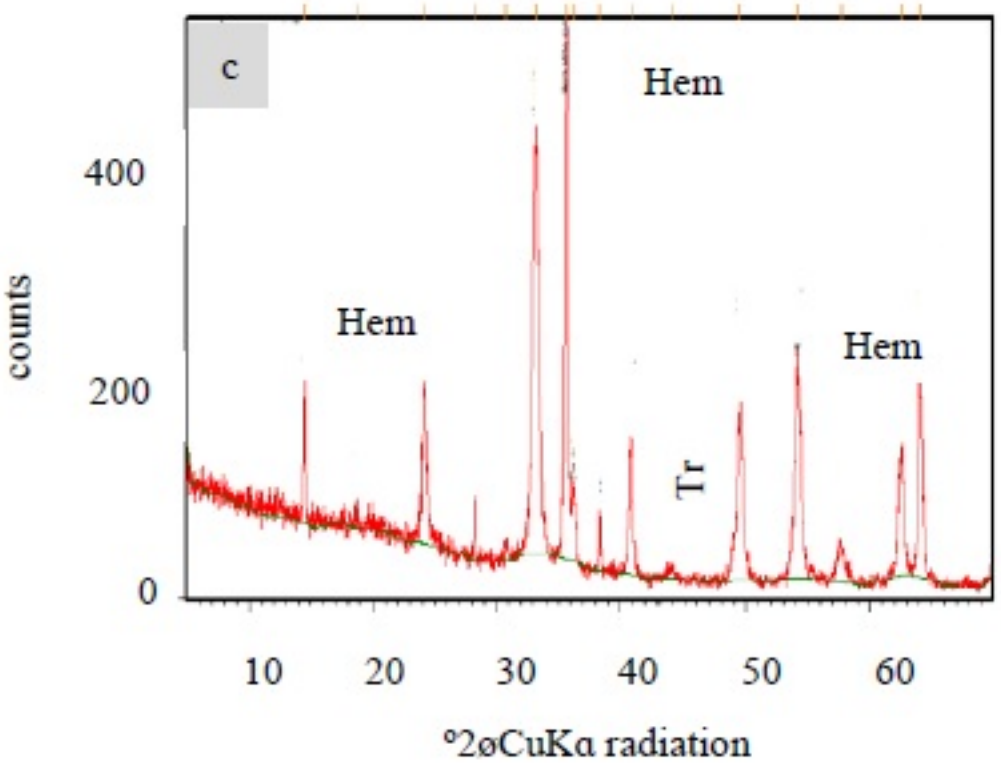
c
Hem
Hem
Hem
Tr
counts
°2øCuKα radiation

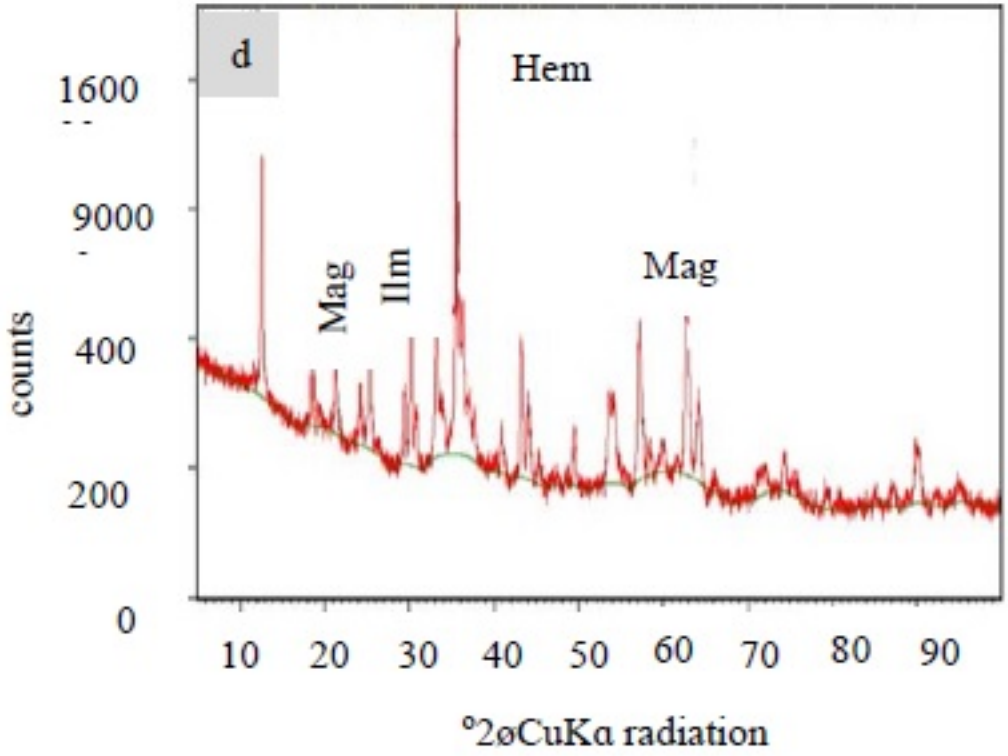
d
Hem
Mag
Ilm
Mag
counts
°2øCuKα radiation

Figure 6.

(a)

Oxide, ferricrete

Lateritization

Protolith, saprolite

Fe_2O_3 wt.%

SiO_2 wt.%

(b)

Oxide, ferricrete

Lateritization

Protolith, saprolite

Al_2O_3 wt.%

SiO_2 wt.%

Loc.1
Loc.2-4
Loc.5
Loc.6
Protolith

(c)

Protolith, saprolite

Lateritization

Oxide, ferricrete

MgO wt.%

SiO_2 wt.%

(d)

Protolith, saprolite

Lateritization

Oxide, ferricrete

MgO wt.%

Fe_2O_3 wt.%

Figure 7.

(a)

NiO wt.%

Fe_2O_3 wt.%

Protolith, saprolite

Lateritization

Oxide, ferricrete

(b)

Total PGE (ppb)

Fe_2O_3 wt.%

Protolith, saprolite

Lateritization

Oxide, ferricrete

Loc.1
Loc.2-4
Loc.5
Loc.6
Protolith

(c)

Total PGE (ppb)

Cr_2O_3 wt.%

Protolith, saprolite

Lateritization

Oxide, ferricrete

(d)

Total PGE (ppb)

NiO wt.%

Protolith, saprolite

Lateritization

Oxide, ferricrete

Figure 8.

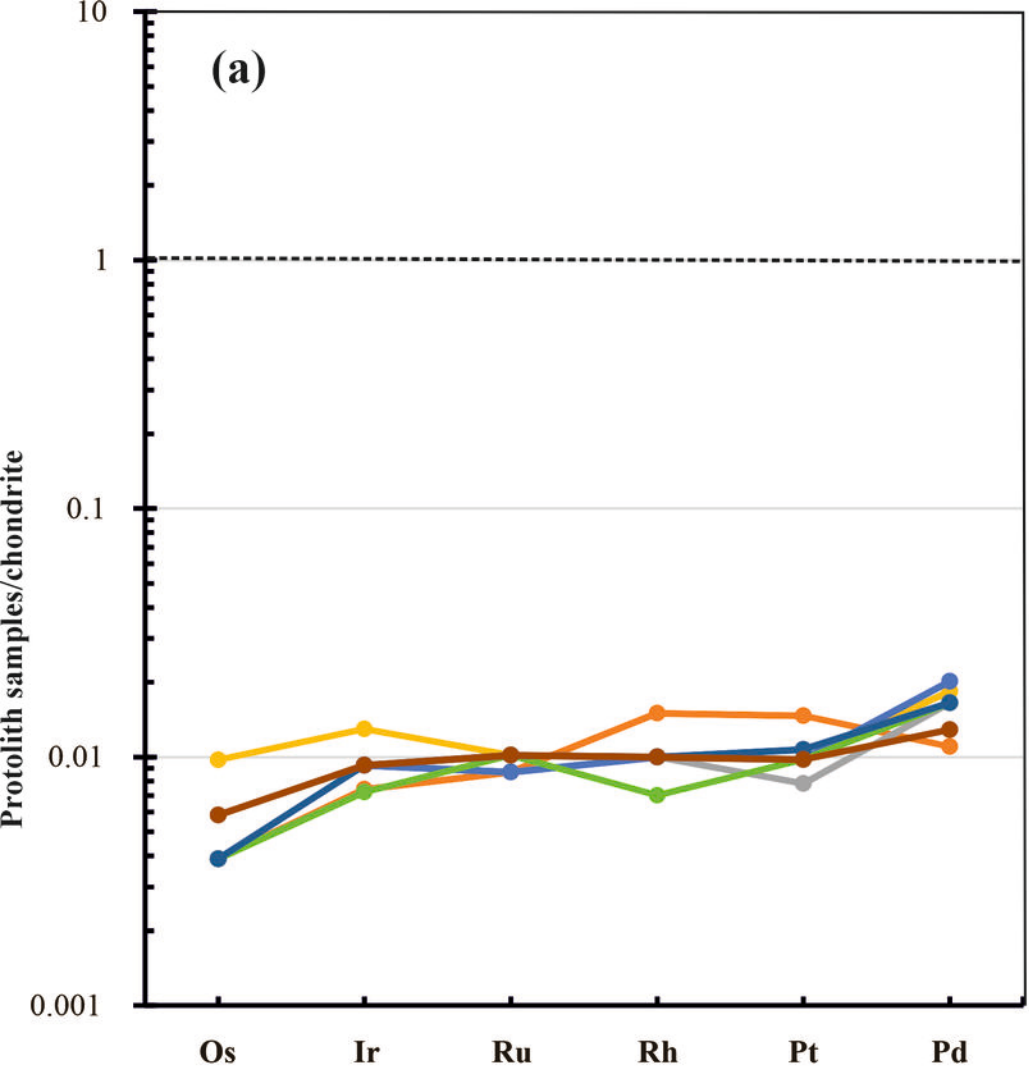
(a)
Protolith samples/chondrite
10
1
0.1
0.01
0.001
Os
Ir
Ru
Rh
Pt
Pd

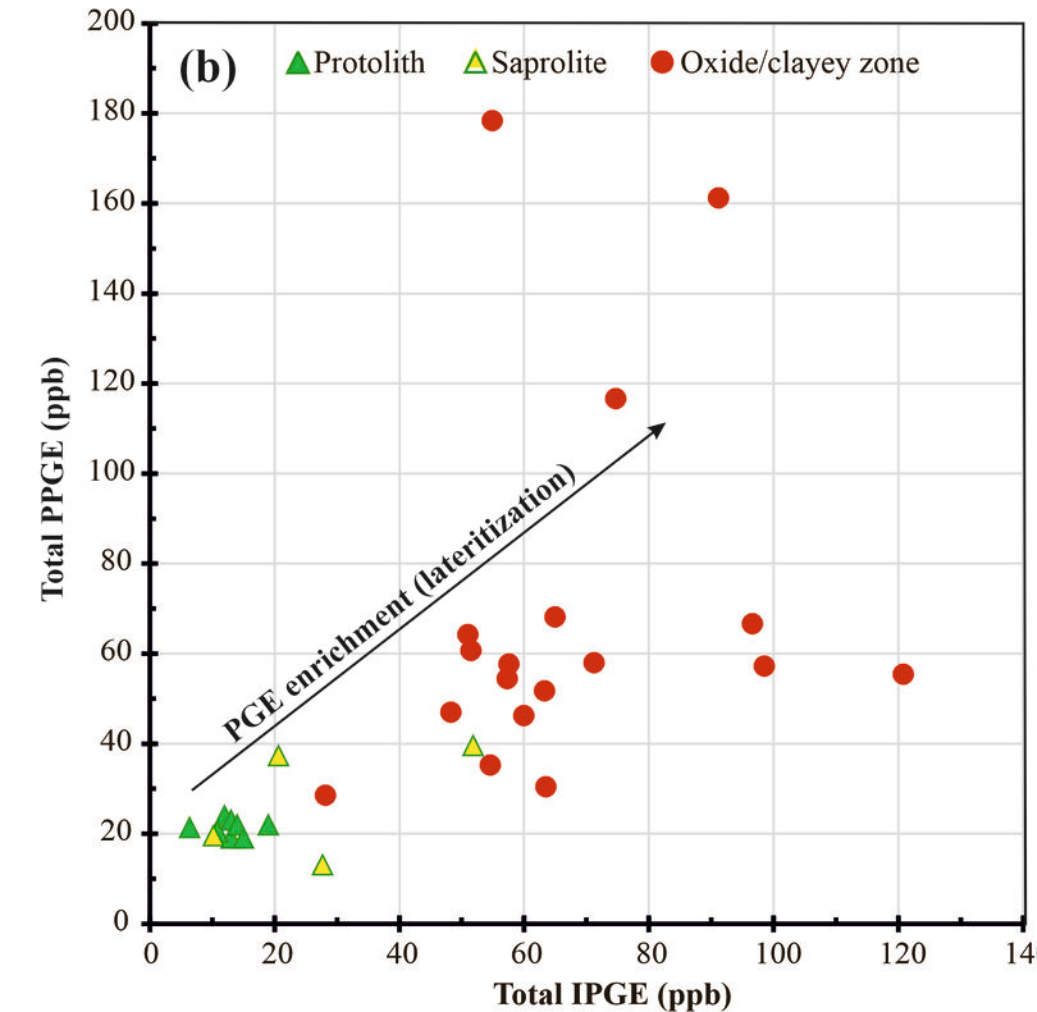
(b)
Protolith
Saprolite
Oxide/clayey zone
PGE enrichment (lateritization)
Total PPGE (ppb)
Total IPGE (ppb)
0
20
40
60
80
100
120
140
160
180
200

Figure 9.

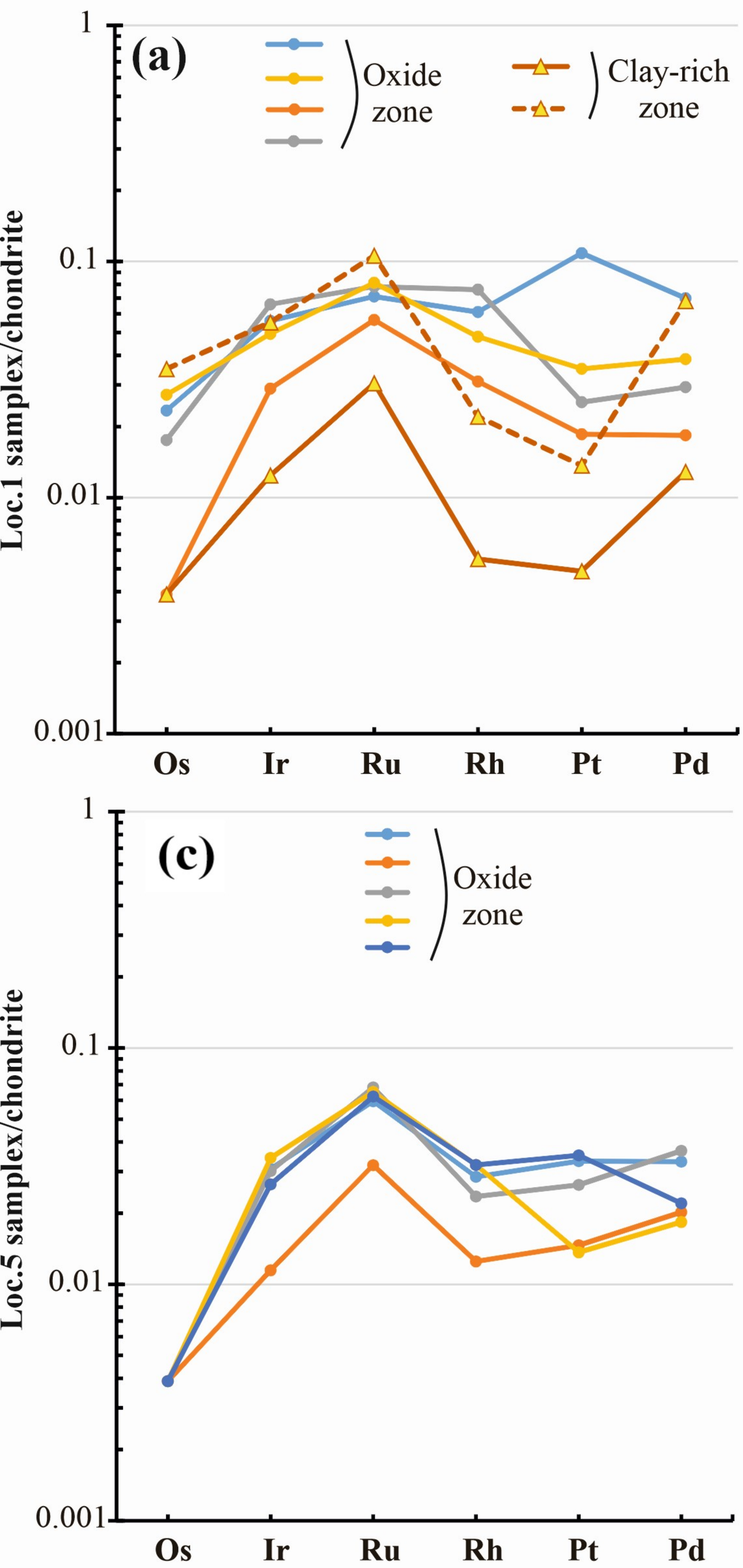
(a)
Oxide zone
Clay-rich zone
Loc.1 samplex/chondrite
1
0.1
0.01
0.001
Os
Ir
Ru
Rh
Pt
Pd

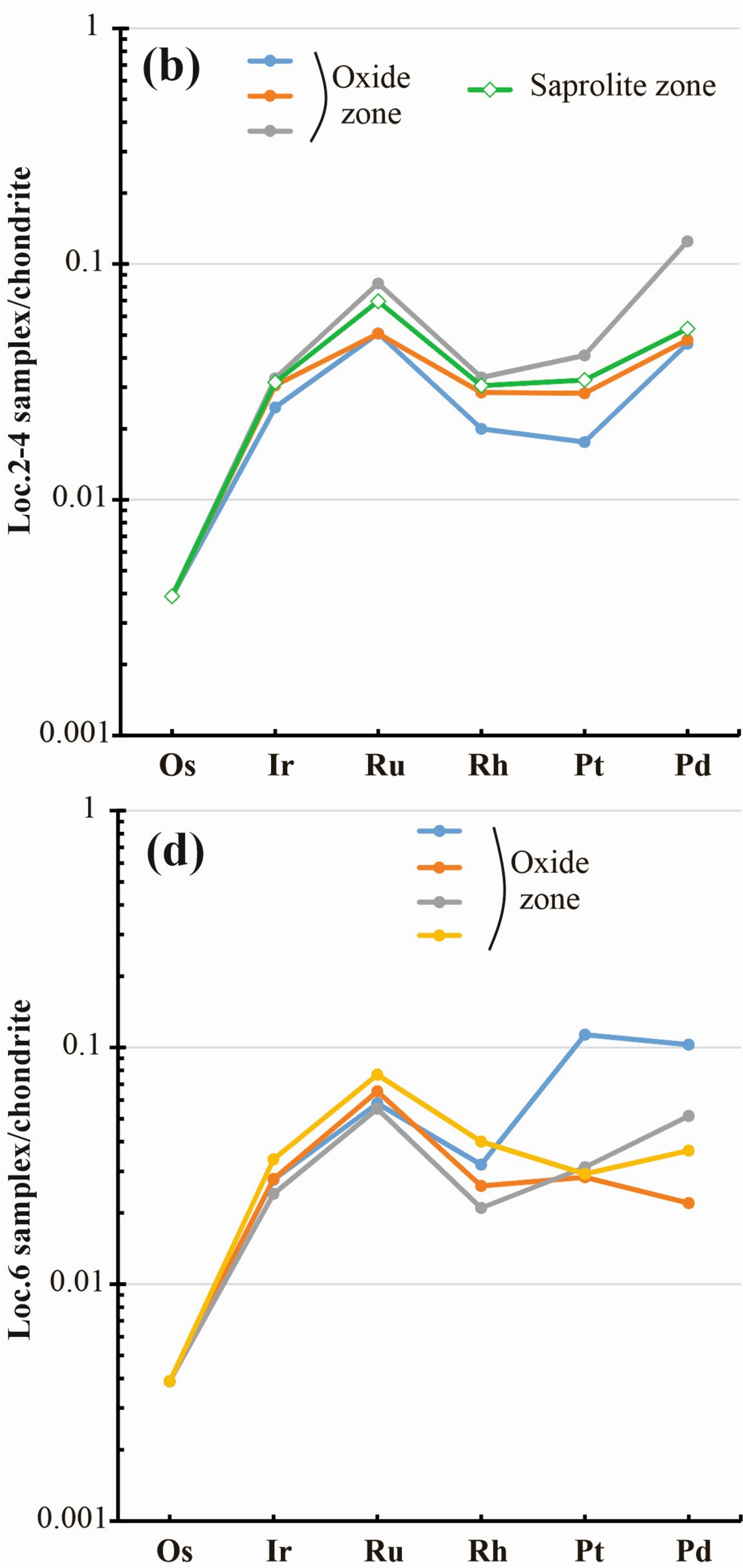
(b)
Oxide zone
Saprolite zone
Loc.2-4 samplex/chondrite
1
0.1
0.01
0.001
Os
Ir
Ru
Rh
Pt
Pd

(c)
Oxide zone
Loc.5 samplex/chondrite
1
0.1
0.01
0.001
Os
Ir
Ru
Rh
Pt
Pd

(d)
Oxide zone
Loc.6 samplex/chondrite
1
0.1
0.01
0.001
Os
Ir
Ru
Rh
Pt
Pd

Figure 10.

Ultramafic Index of Alteration (UMIA)
(molar %)

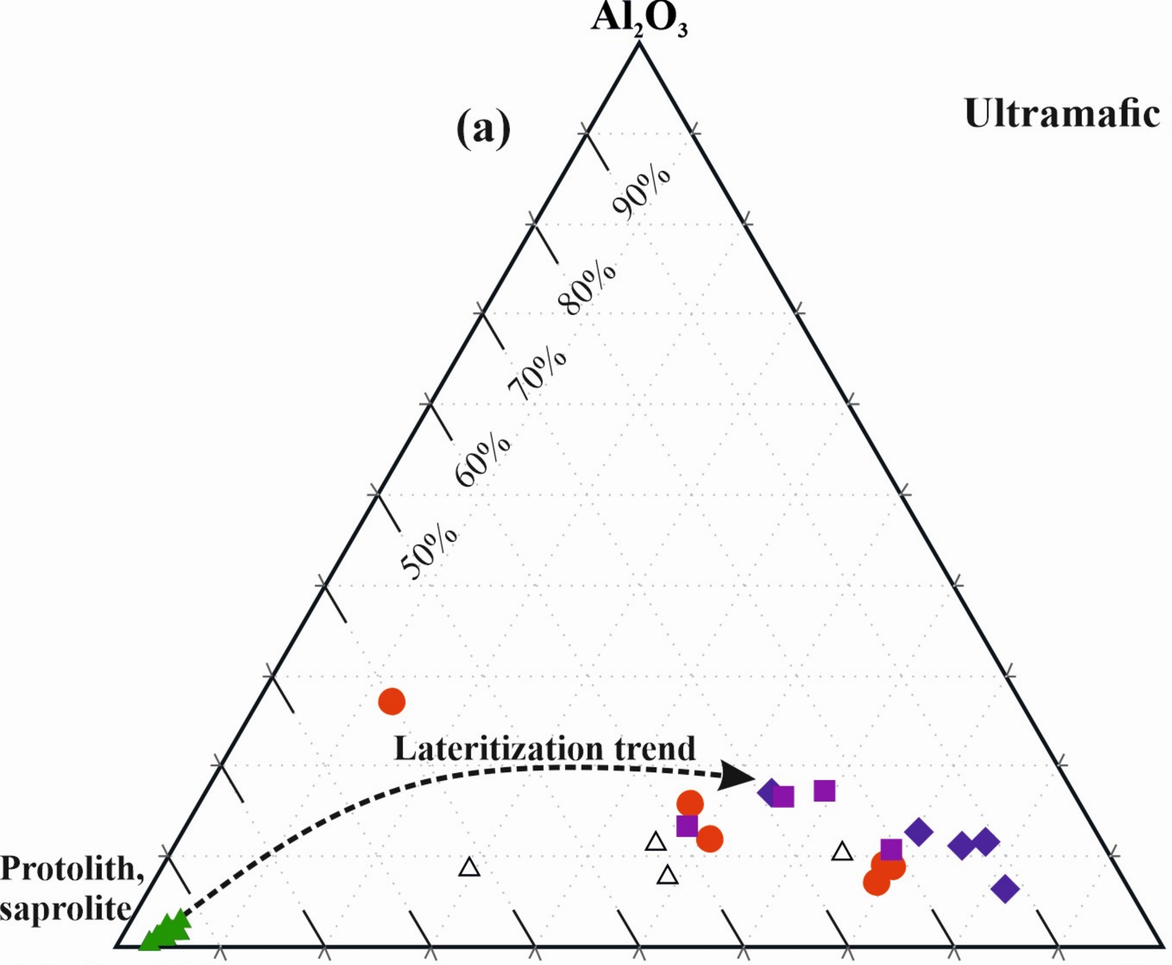

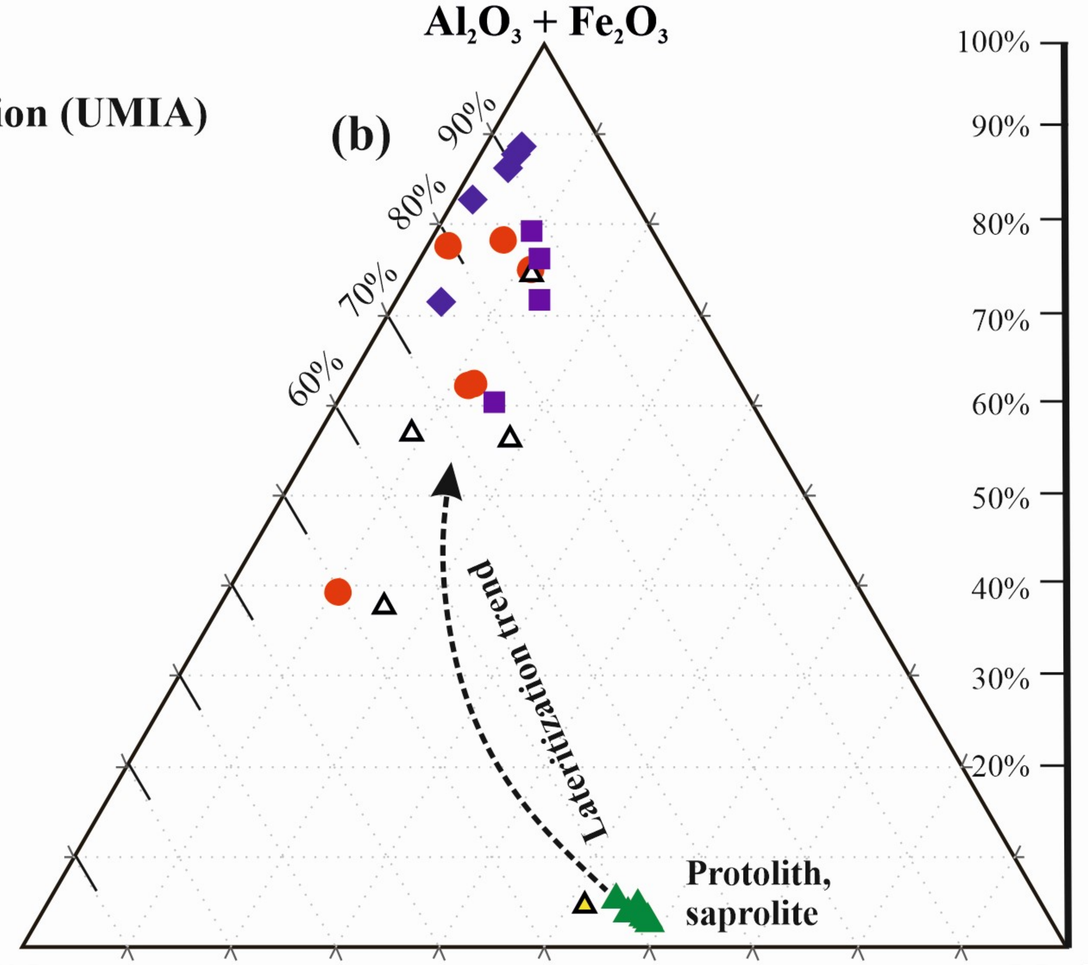

Loc.1
Loc.2-4
Loc.5
Loc.6
Saprolite
Protolith

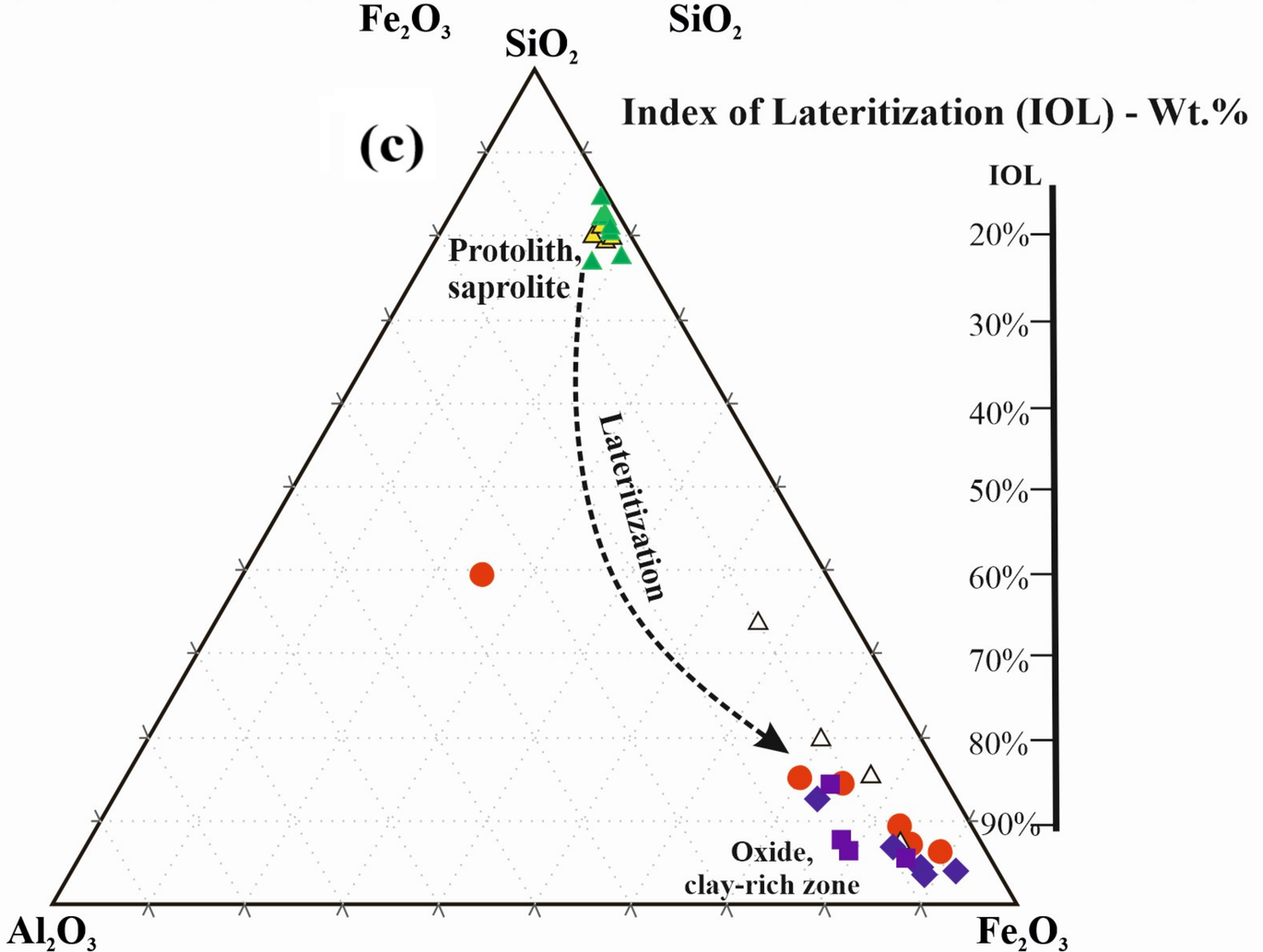

Figure 11.

(a)

Fe_2O_3 wt.%

Al_2O_3 wt.%

Lateritization trend

(b)

NiO wt.%

Co_3O_4 wt.%

Lateritization trend

Loc. 1
Loc. 2-4
Loc. 5
Loc. 6
Saprolite
Protolith

(c)

Cr_2O_3 wt.%

UMIA

Lateritization trend

(d)

Total PGE (ppb)

UMIA

Lateritization trend

Figure 12.

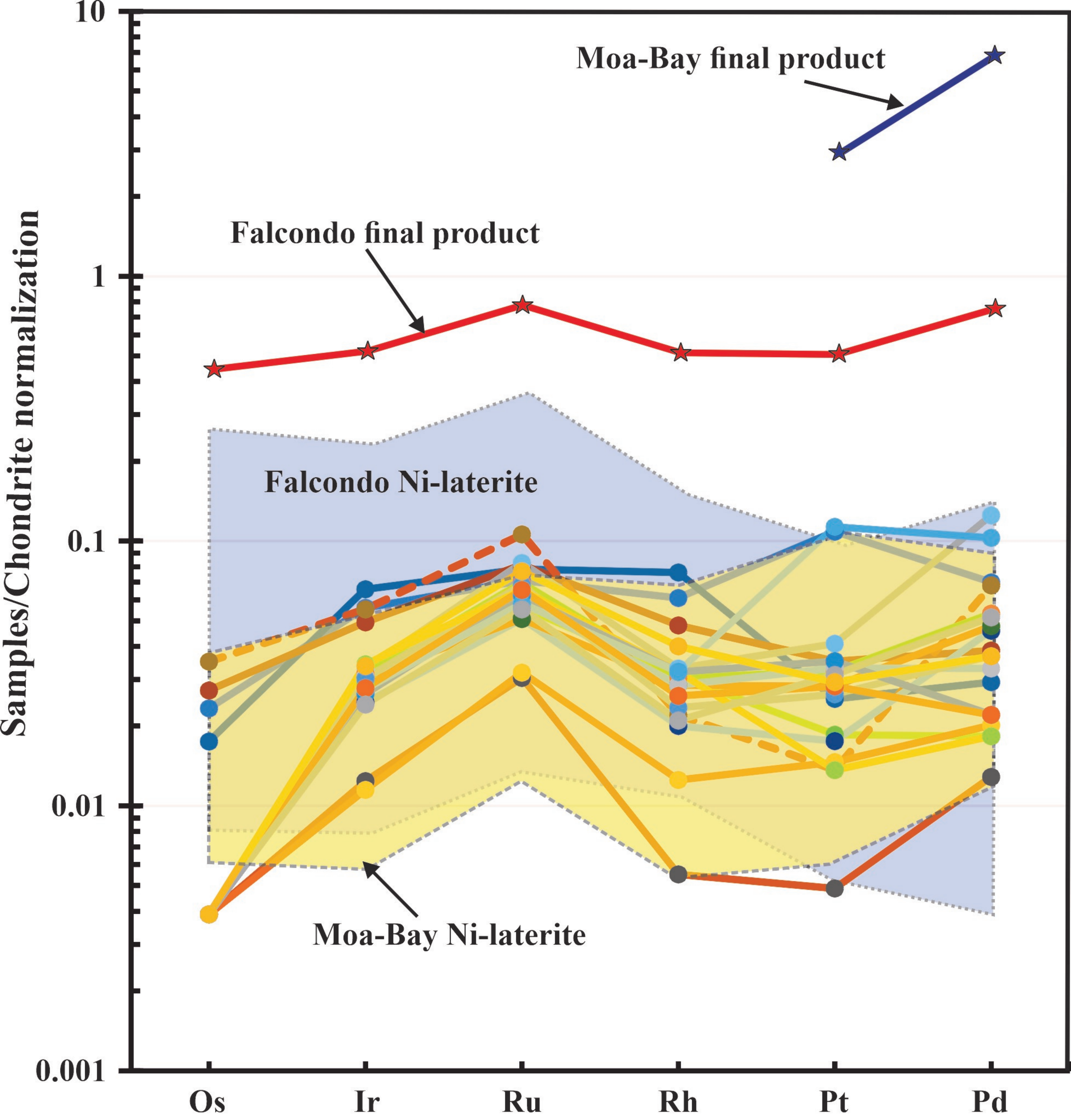
Samples/Chondrite normalization
10
1
0.1
0.01
0.001
Moa-Bay final product
Falcondo final product
Falcondo Ni-laterite
Moa-Bay Ni-laterite
Os
Ir
Ru
Rh
Pt
Pd

Table 1

Zone			Protolith					Saprolite	
Loc #	loc-1	loc-1	loc-1	loc-2	loc-5	loc-6	loc-2	loc-3	loc-4
SiO_2	37.67	37.11	36.74	37.17	37.11	36.12	38.96	40.66	36.92
Al_2O_3	0.92	0.94	1.12	2.76	0.67	0.75	0.75	0.91	0.38
Fe_2O_3(T)	8.28	7.21	9.60	8.46	7.22	7.77	7.78	9.16	6.39
MnO	0.16	0.13	0.12	0.20	0.10	0.12	0.11	0.12	0.09
MgO	35.78	36.57	35.33	32.87	37.63	35.16	36.43	31.91	37.00
CaO	1.60	0.58	0.68	2.82	0.05	0.67	0.76	1.19	3.25
Na_2O	n.d.	n.d.	n.d.	0.01	n.d.	0.02	0.01	0.01	0.01
K_2O	0.01	0.02	0.01	0.02	0.00	0.09	0.01	0.03	0.01
TiO_2	0.02	0.02	0.03	0.08	0.01	0.01	0.01	0.02	0.01
P_2O_5	0.01	0.01	n.d.	n.d.	n.d.	0.00	0.01	0.05	0.04
Cr_2O_3	0.45	0.36	0.31	0.37	0.29	0.23	0.35	0.46	0.32
NiO	0.16	0.15	0.18	0.12	0.18	0.19	0.29	0.33	0.25
Co_3O_4	0.01	0.01	0.01	0.01	0.01	0.01	0.01	0.02	0.01
LOI	15.72	16.18	15.81	15.67	15.20	15.10	14.60	15.88	15.86
Total	100.79	99.29	99.95	100.56	98.48	96.25	100.09	100.74	100.54
UMIA	4	3	5	5	3	4	3	4	3
IOL	4	3	5	5	3	4	4	4	3
PGE (ppb)									
Os	<2	<2	5	<2	<2	3	<2	<2	< 2
Ir	4	5	7	4	5	5	5	5	11
Ru	6	6	7	7	7	7	6	16	41
Rh	3	2	2	1	2	2	2	2	5
Pt	15	8	10	10	11	10	10	21	23
Pd	6	9	10	9	9	7	11	14	12
Au	n.d.	n.d.	n.d.	3	n.d.	n.d.	n.d.	5	1
∑ PGE	34	30	41	31	34	34	34	58	91
∑ IPGE	10	11	19	11	12	15	11	21	52
∑ PPGE	24	19	22	20	22	19	23	37	40
Pd/IrN	1.49	1.78	1.42	2.18	2.29	1.78	1.39	3.02	1.10
Ru/PtN	0.59	1.11	1.04	0.89	1.04	0.95	1.04	1.13	2.65

Table 2

Zone	oxide				clay-rich		oxide				oxide					oxide			
Loc #	loc-1						loc-2-4					loc-5				loc-6			
SiO_2	7.32	12.24	4.35	2.23	8.42	27.06	26.93	16.62	6.14	12.55	5.75	3.67	10.84	3.08	4.01	6.59	5.43	10.20	4.78
Al_2O_3	7.11	9.28	4.37	1.70	6.54	24.49	8.00	8.93	7.17	6.11	7.93	4.02	12.34	6.65	6.86	12.13	12.10	8.70	7.46
Fe_2O_3 (T)	33.31	62.70	50.53	31.14	72.82	16.82	45.14	59.20	71.69	63.11	71.13	85.50	63.02	75.87	78.18	65.99	67.49	52.36	73.39
MnO	0.54	0.18	0.65	2.52	0.18	0.18	0.46	0.31	0.26	0.19	0.10	0.04	0.11	0.05	0.12	0.32	0.19	0.17	0.33
MgO	1.93	3.57	1.10	1.37	0.37	3.80	6.18	2.81	3.07	6.14	0.40	0.69	1.03	0.70	0.87	4.14	3.37	3.94	2.48
CaO	24.30	1.33	18.59	30.31	0.20	1.30	0.61	0.39	0.47	0.32	0.06	0.07	0.29	0.51	0.92	1.88	1.28	6.36	2.81
Na_2O	0.06	0.06	0.04	0.21	0.10	0.14	0.06	0.05	0.01	0.01	0.45	0.01	0.09	0.08	0.20	0.03	0.05	0.17	0.05
K_2O	0.02	0.03	0.01	0.01	0.01	0.84	0.05	0.02	0.02	0.03	0.10	0.01	0.01	0.01	0.01	0.01	0.01	0.02	0.01
TiO_2	0.08	0.09	0.06	0.03	0.11	0.57	0.21	0.19	0.06	0.26	0.24	0.11	0.11	0.13	0.17	0.16	0.14	0.04	0.07
P_2O_5	0.04	0.01	0.01	0.01	0.03	0.01	0.01	0.03	0.06	0.05	0.12	0.08	0.06	0.09	0.06	0.01	0.01	0.01	0.01
Cr_2O_3	2.48	3.36	1.96	2.51	2.04	11.44	3.65	4.39	3.87	3.40	3.69	3.27	3.77	5.70	2.69	3.17	5.35	3.46	2.12
NiO	0.04	0.16	0.03	0.07	0.05	0.12	0.10	0.11	0.11	0.50	0.07	0.02	0.06	0.01	0.05	0.10	0.08	0.21	0.20
Co_3O_4	0.51	1.49	0.58	1.14	0.38	2.01	1.41	0.79	1.67	1.85	0.21	0.18	0.76	0.11	0.31	1.18	0.65	2.85	1.34
LOI	22.41	6.37	16.67	25.62	8.02	12.59	7.11	4.99	5.17	6.06	10.42	3.23	10.67	10.46	4.87	4.87	4.27	10.65	4.48
Total	100.15	100.86	98.94	98.88	99.28	101.37	99.92	98.83	99.77	100.58	100.67	100.90	103.16	103.45	99.32	100.58	100.42	99.15	99.53
UMIA	62	62	78	75	78	39	38	57	74	56	83	88	71	89	86	71	76	61	79
IOL	74	71	86	80	86	53	41	64	83	60	95	94	86	99	96	85	91	69	89
PGE (ppb)																			
Os	12	< 2	9	14	< 2	18	< 2	< 2	< 2	< 2	< 2	< 2	< 2	< 2	< 2	< 2	< 2	< 2	< 2
Ir	30	16	36	27	7	30	13	17	18	17	17	6	16	19	14	15	15	13	18
Ru	49	39	54	56	21	73	35	35	57	48	41	22	47	45	43	40	45	38	53
Rh	12	6	15	10	1	4	4	6	7	6.1	6	3	5	6	6	6	5	4	8

Pt	111	19	26	36	5	14	18	29	42	33	34	15	27	14	36	116	29	32	30
Pd	38	10	16	21	7	37	25	26	68	29	18	11	20	10	12	56	12	28	20
Au	2	2	4	3	1	15	3	2	8.6	0.8	3	3	1	1	1	1	1	1	1
∑ PGE	252	90	156	163	41	176	95	112	191	133	115	57	115	94	112	233	106	115	129
∑ IPGE	91	55	99	97	28	121	48	52	75	65	58	28	63	64	57	55	60	51	71
∑ PPGE	161	35	57	67	13	55	47	61	117	68	58	29	52	30	54	178	46	64	58
Pd/Ir N	1.25	0.64	0.45	0.78	1.04	1.23	1.86	1.56	3.81	1.69	1.07	1.76	1.22	0.54	0.83	3.72	0.79	2.13	1.09
Ru/Pt N	0.66	3.05	3.09	2.31	6.24	7.75	2.89	1.79	2.02	2.16	1.79	2.18	2.59	4.77	1.77	0.51	2.31	1.76	2.62